Characterization of a K + Induced Conformational Switch in a Human Telomeric DNA Oligonucleotide Using 2Aminopurine Fluorescence

ARTICLE *in* BIOCHEMISTRY · JANUARY 2010

Impact Factor: 3.02 · DOI: 10.1021/bi901357r · Source: PubMed

4 AUTHORS, INCLUDING:

Luigi Petraccone
University of Naples Federico II
56 PUBLICATIONS **833** CITATIONS
SEE PROFILE

John O Trent
University of Louisville
131 PUBLICATIONS **5,431** CITATIONS
SEE PROFILE

Jonathan B Chaires
University of Louisville
195 PUBLICATIONS **11,480** CITATIONS
SEE PROFILE

BIOCHEMISTRY
including biophysical chemistry & molecular biology
Article

Biochemistry **2010,** *49,* 179–194 179
DOI: 10.1021/bi901357r

Characterization of a K^+-Induced Conformational Switch in a Human Telomeric DNA Oligonucleotide Using 2-Aminopurine Fluorescence†

Robert D. Gray,‡ Luigi Petraccone,‡,§ John O. Trent,‡ and Jonathan B. Chaires*,‡

‡*James Graham Brown Cancer Center, University of Louisville, Louisville, Kentucky 40202 and* §*Department of Chemistry "P. Corradini", University of Naples Federico II, 80126 Naples, Italy*

Received August 5, 2009; Revised Manuscript Received December 2, 2009

ABSTRACT: Human telomeric DNA consists of tandem repeats of the DNA sequence d(GGGTTA). Oligodeoxynucleotide telomere models such as d[A(GGGTTA)$_3$GGG] (Tel22) fold in a cation-dependent manner into quadruplex structures consisting of stacked G-quartets linked by d(TTA) loops. NMR has shown that in Na^+ solutions Tel22 forms a "basket" topology of four antiparallel strands; in contrast, Tel22 in K^+ solutions consists of a mixture of unknown topologies. Our previous studies on the mechanism of folding of Tel22 and similar telomere analogues utilized changes in UV absorption between 270 and 325 nm that report primarily on G-quartet formation and stacking showed that quadruplex formation occurs within milliseconds upon mixing with an appropriate cation. In this study, we assess the dynamics and equilibria of folding of specific loops by using Tel22 derivatives in which the dA residues were serially substituted with the fluorescent reporter base, 2-aminopurine (2-AP). Tel22 folding induced by Na^+ or K^+ assessed by changes in 2-AP fluorescence consists of at least three kinetic steps with time constants spanning a range from milliseconds to several hundred seconds. Na^+-dependent equilibrium titrations of Tel22 folding could be approximated as a cooperative two-state process. In contrast, K^+-dependent folding curves were biphasic, revealing that different conformational ensembles are present in 1 and 30 mM K^+. This conclusion was confirmed by ^{1}H NMR. Molecular dynamics simulations revealed a K^+ binding pocket in Tel22 located near dA1 that is specific for the so-called hybrid-1 conformation in which strand 1 is in a parallel arrangement. The possible presence of this topologically specific binding site suggests that K^+ may play an allosteric role in regulating telomere conformation and function by modulating quadruplex tertiary structure.

Recent analysis of the human genome reveals the presence of G-rich sequences that have a propensity to fold into quadruplex structures (*1*, *2*). These G-rich regions include telomeres, certain transcriptional promoters, and immunoglobulin switch regions. Telomeres are nucleoprotein structures located at the ends of chromosomes (for a review, see ref *3*). In humans, telomeric DNA contains 30−50 tandem repeats of the sequence d(TTAGGG) that exist as a single-stranded overhang at the 3′ end of chromosomes (*4*). Telomeres maintain chromosomal integrity during cell division (*3*, *5*, *6*); the inability of most cell types to replace telomeric DNA during replication eventually results in cell death (*7*). Most cancer cells, by virtue of their ability to produce telomerase, are capable of maintaining telomeric DNA, thereby contributing to cellular immortality (*8*). Recent evidence suggests that these G-rich telomeric DNA sequences may fold into G-quadruplex structures in vivo (*9*).

A number of recent reviews summarize the details of quadruplex structure and function (*10*−*13*). In brief, quadruplex DNA consists of stacked planar, cyclic arrays of four dG residues linked by Hoogsteen hydrogen bonds involving the N1, N2, N7, and O6 atoms of each quartet. Quadruplex stability is markedly enhanced by coordination of a monovalent cation such as K^+ or Na^+ to the guanine O6 atoms that protrude into the central cavity of the G-tetrad. Individual G-quartets stack to form a structure with a central channel that contains a monovalent cation chelated either between quartets or within the center of the macrocyclic ring.

Oligonucleotides containing G-quadruplexes are notable for their conformational diversity; indeed, changes in cation, loop sequence, or terminal bases may result in changes in quadruplex topology (*13*). A 22-nucleotide model of the human telomeric sequence utilized in the experiments reported here, d[AG$_3$(T$_2$AG$_3$)$_3$] (Tel22),[1] has been shown to exist in a different conformations under different conditions. From NMR data, Wang et al. (*14*) deduced that Tel22 in a Na^+-containing solution folds into a unimolecular "basket". This topology, depicted in Figure 1A, consists of an antiparallel arrangement of four strands with lateral loops connecting strand 1 to strand 2 and strand 3 to strand 4, and a diagonal loop connecting strand 2 to strand 3. In contrast, Tel22 crystallized in K^+ folds into an all-parallel

†Supported by Grant GM 077422 from the National Institutes of Health (NIH) and the James Graham Brown Foundation. NMR spectra were recorded at the James Graham Brown Cancer Center NMR facility, supported in part by NIH Grant P20RR018733 from the National Center for Research Resources and National Science Foundation EPSCoR Grant EPS-0447479.

*To whom correspondence should be addressed. Phone: (502) 852-1172. Fax: (502) 852-1153. E-mail: jbchai01@gwise.louisville.edu.

[1]Abbreviations: 2-AP, 2-aminopurine; Bu$_4$AmP, tetrabutylammonium phosphate; cps, fluorescence intensity in counts per second; DSS, 4,4-dimethyl-4-silapentane-1-sulfonic acid; MD, molecular dynamics; FRET, fluorescence resonance energy transfer; NOE, nuclear Overhauser effect; PDB, Protein Data Bank; SASA, solvent accessible surface area; SVD, singular-value decomposition; Tel22, d[A(GGGTTA)$_3$GGG]; TT-Tel22-A, d[TT(GGGTTA)$_3$GGGA]; TT-Tel22, d[TT(GGGTTA)$_3$GGG].

Published on Web 12/04/2009

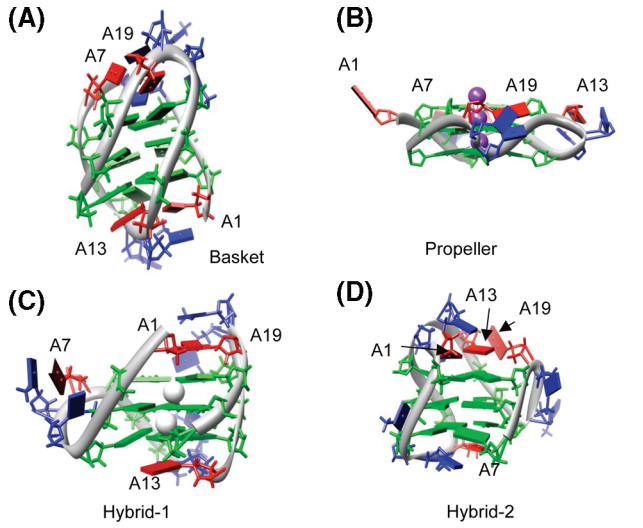

FIGURE 1: Topological variants of G-quadruplexes formed under different conditions for the human telomeric oligodeoxynucleotide d[A(GGGTTA)$_3$GGG] showing positions of loop adenine residues (red slabs). The basket structure is from the NMR-determined structure [PDB entry 143D (*14*)]. The propeller structure was determined by X-ray crystallography [PDB entry 1KF1 (*15*)]. The hybrid-1 and hybrid-2 structures were modeled from NMR structures 2HY9 (*43*) and 2JPZ (*44*), respectively, as described in Experimental Procedures. Green slabs represent G residues and blue slabs T residues. The diagrams were created using the molecular graphics program Chimera (*48*).

structure in which the connecting loops form a "propeller"-like structure (Figure 1B) (*15*). However, NMR, as well as a variety of other biophysical techniques, indicates that Tel22 in K^+ solutions exists as an undefined mixture of structures (*16*, *17*). Suggested topologies include a "chair" structure (four antiparallel strands connected by three lateral loops) and topologies in which there is a propeller-type loop connecting strand 1 to strand 2 or strand 3 to strand 4 (Figure 1C,D) (*18*, *19*). The latter structures in which the first two stands or the last two strands are in a parallel topology are the predominant conformers in K^+ solutions of human telomeric sequences modified by addition of 5′ and 3′ nucleotides (*17*, *20*, *21*). The former has been termed a hybrid-1 structure and the latter a hybrid-2 structure.

We recently compared the folding kinetics of oligonucleotides that form well-defined basket and hybrid-1 structures, Tel22 in Na^+ and TT-Tel22-A {d[TT(GGGTTA)$_3$A]} in K^+ using rapid scanning stopped-flow spectrophotometry to assess the extent of quadruplex formation (*22*). For both of these sequences, a single-exponential process with sequence-dependent time constants of 20−60 ms in 50 mM KCl was observed. In contrast, in 100 mM NaCl, folding of both sequences consisted of three steps with relaxation times in the millisecond to second range. These kinetic data are consistent with reaction sequences 1 and 2:

$$U + 2K^+ \leftrightarrow I \rightarrow F{-}K_2 \quad (1)$$

$$U + 3Na^+ \leftrightarrow I1 \rightarrow I2 \rightarrow F{-}Na_3 \quad (2)$$

where U represents an ensemble of unfolded conformers, I is an intermediate, and F represents the folded quadruplex structure.

Folding equilibria for these oligonucleotides were cooperative with respect to cation concentration and exhibited midpoint cation concentrations 10−20-fold lower for K^+ than for Na^+ (*22*). This higher apparent affinity of K^+ is consistent with the results of Hud et al. (*23*), who showed that the preference for K^+ compared to Na^+ coordination results from a higher desolvation energy required for its incorporation of Na^+ into the quadruplex central channel.

In a subsequent study (*24*), we found that exchange of Na^+ for K^+ is also a multistep process, consisting of three relaxations as determined by changes in the CD spectrum accompanying the cation-induced rearrangement shown in eq 3:

$$F{-}Na_3 \rightarrow I1 \leftrightarrow I2 \leftrightarrow F{-}K_2 \quad (3)$$

The changes in UV absorption in the 275−320 nm range that were used to monitor the folding transitions in the studies described above most likely report predominately on G-quartet formation and may be less sensitive to loop conformation. Because the loops of Tel22 consist of dTTA triads, we reasoned that the fluorescent adenine analogue, 2-aminopurine (2-AP), could be a sensitive indicator of loop conformational changes. 2-AP has been utilized extensively as a probe of oligonucleotide folding (*25*−*29*). For example, previous studies from our laboratory showed that the fluorescence properties of Tel22 analogues with 2-AP substituted serially for the four dA residues are sensitive to quadruplex folding topology (*27*). In addition, factors that influence 2-AP fluorescence are well-characterized, thus making 2-AP-substituted Tel22 analogues excellent probes of loop structure (*30*−*36*).

EXPERIMENTAL PROCEDURES

Materials. Synthetic oligodeoxynucleotides were obtained from IDT, Inc. (Coralville, IA). Stock solutions of 500−750 μM in strand concentration were prepared by dissolving the desalted, lyophilized oligonucleotide in 10 mM Bu_4AmP and 1 mM EDTA (pH 7.0) (termed folding buffer). Oligonucleotide concentrations were determined from their absorbance at 260 nm using extinction coefficients supplied by IDT (228.5 mM^{-1} cm^{-1} for Tel22 and 215.5 mM^{-1} cm^{-1} for the Tel22 2-AP derivatives). NaCl, KCl, 2-aminopurine, monobasic tetrabutylammonium phosphate, and tetrabutylammonium hydroxide were from Sigma (St. Louis, MO). Stock NaCl and KCl solutions for titration experiments were prepared in folding buffer.

Equilibrium Measurements of Cation-Induced Folding. The dependence of the extent of folding on cation concentration was assessed by measuring changes in UV absorption, CD, and, for the 2-AP derivatives, fluorescence emission intensity. The spectrophotometric titrations were conducted as previously described (*22*). The absorbance at 295 nm or fluorescence intensity at 370 nm was allowed to equilibrate between additions of cation (usually 5−10 min).[2] CD spectra were recorded with a Jasco J-810 spectropolarimeter equipped with a magnetic mixer and a Peltier thermostat (Jasco USA, Easton, MD). Fluorometric experiments were conducted at 25 °C in a 1 cm × 1 cm quartz cuvette with a Fluoromax-3 spectrofluorometer equipped with a magnetic mixer and a fluorescence polarization accessory (HORIBA Jobin Yvon Inc., Edison, NJ). 2-AP-containing oligodeoxynucleotides were excited at 305 nm (2 nm bandwidth), and emission spectra were measured at 1 nm intervals from 320 to 460 nm using a 5 nm bandwidth. Fluorescence intensities were corrected for instrumental response using Fluoromax software,

[2]After completion of this paper, we observed additional very slow changes in UV absorption and ellipticity in the spectral region between 220 and 265 nm that occurred over a period of up to 8 h when KCl was mixed at room temperature with unfolded Tel22. The implications of these slow changes are currently under investigation.

by subtracting a buffer spectrum. We corrected emission spectra for day-to-day variation in excitation lamp intensity by normalizing to the intensity of the 342 nm Raman scattering peak of water. Fluorescence intensities are presented in units of counts per second per micromolar oligonucleotide.

Analysis of Titration Data. A two-state model for cation-induced folding of monomolecular G-quadruplexes is described by the equation $U + nM \leftrightarrow FM_n$, where U and F designate the unfolded and folded states of the oligonucleotide, respectively, and M is either Na^+ or K^+. The titration curves were fit to a modified Hill equation (eq 4) corresponding to

$$S_i = (S_U - S_F)[M]_i^n/(K_{0.5}{}^n + [M]_i^n) + S_F \quad (4)$$

where S_i is the observed spectroscopic signal (e.g., absorbance, CD, or fluorescence) determined at cation concentration i at the wavelength of maximal signal change. The parameters S_U and S_F (representing the signal of the unfolded and folded states, respectively), $K_{0.5}$ (the midpoint cation concentration), and the Hill coefficient n were optimized using the nonlinear least-squares module in Origin version 7.0 (OriginLab Corp., Northampton, MA). The two-state model is an oversimplification [as shown in our previous work (*22*) and amplified below], but it is useful for qualitative comparison of the folding isotherms.

Spectroscopic Intermediates. Data matrices consisting of the wavelength-dependent cation titrations and the wavelength-dependent kinetic data were analyzed as previously described (*22*) using the method of singular-value decomposition (SVD) to assess the presence of spectroscopic intermediates and depict their time- or cation concentration-dependent profiles (*37*, *38*). The application of SVD to multistate DNA transitions has been previously described (*39*, *40*); the interested reader is referred to these references for more details. The SVD data analysis was conducted with either MatLab version 7.1 (The MathWorks, Natick, MA) or Specfit/32 version 3.0.39 (Spectrum Software Associates, Marlborough, MA). The spectra and concentration profiles of the significant species in the equilibrium titrations were determined using the "model-free evolving factor analysis" module in Specfit/32 (*41*).

Folding Kinetics. Kinetic constants for cation-induced quadruplex formation were determined by rapid scanning stopped-flow spectrophotometry using the instrument manufactured by OLIS, Inc. (Bogart, GA), as previously described (*22*). The kinetics of changes in 2-AP fluorescence were determined with the Fluoromax3 fluorometer equipped with a stopped-flow cuvette (SFA-20, High-Tech Scientific, Bradford-on-Avon, U.K.) or by manual addition of 3 M KCl or 3 M NaCl to the oligonucleotide solution while the solution was being vigorously stirred with an in-cuvette magnetic stirrer. The nominal dead times (the time interval between the addition of cation and the initiation of data collection) were ~0.1 and ~5 s for the stopped-flow and manual mixing methods, respectively. Fluorometric determinations of the kinetics of exchange of Na^+ by K^+ were assessed by rapidly adding KCl to a solution of the oligonucleotide prefolded in NaCl as previously described (*24*). The progress curves for the folding and cation exchange reactions generally consisted of one or two exponentials as described by eq 5

$$y(t) = y_0 + A_1 \exp(-t/\tau_1) + A_2 \exp(-t/\tau_2) \quad (5)$$

where $y(t)$ is the fluorescence intensity at time t, y_0 is the final equilibrium value of the fluorescence intensity, τ_1 and τ_2 are the relaxation times, and A_1 and A_2 are the corresponding signal amplitudes at time zero. The values of y_0, A_i, and τ_i were optimized by fitting the experimentally determined progress curves to eq 5 using the nonlinear least-squares module in Origin version 7.0.

Fluorescence Polarization. Steady-state fluorescence polarization values (P) of the unfolded and folded 2-AP oligonucleotides were determined at 25 °C with excitation at 305 nm and emission at 370 nm in a 1 cm × 1 cm quartz cuvette using the SpectraMax-3 fluorometer in polarization mode. Folding was initiated by rapid addition of the salt from 3 M stock solutions of either NaCl or KCl in folding buffer to a stirred solution of the unfolded oligonucleotide. P was determined at intervals of 6.7 s for 2000 s. P values for the unfolded oligonucleotide were estimated by averaging at least 100 successive measurements acquired before addition of salt and for the folded oligonucleotide by averaging at least 500 measurements obtained after addition of salt. The standard deviations of the mean P value were ±0.002−0.005. Net changes in P were determined by subtracting the average P for the folded oligonucleotide from that of the unfolded oligonucleotide.

NMR Experiments. Tel22 (179 μM) was dissolved in water with 10% D_2O and 50 μM DSS titrated to pH 6.5 with HCl. NMR spectra were recorded at 18.8 T on a four-channel Varian (Palo Alto, CA) Inova spectrometer using an inverse triple-resonance HCN probe. The intense solvent peak was suppressed using the Watergate sequence (*42*). The acquisition time was 1.5 s, and the recycle time was 3 s. The data were zero-filled once and apodized using an unshifted Gaussian function and a 2 Hz line broadening exponential function. Chemical shifts were referenced to internal DSS. Spectra were recorded at 10 and 25 °C in the absence of K^+ and in the presence of 0.75, 1.5, and 37 mM K^+.

Molecular Dynamics Calculations and Modeling. Starting structures of the hybrid-1 and hybrid-2 conformations were generated from the coordinates of the reported NMR structures [PDB entries 2HY9 (*43*) and 2JPZ (*44*)]. Two K^+ ions were placed between the adjacent G-tetrad planes in each quadruplex structure. The standard parm99.dat Amber force field was used and was modified using the frcmod.parmbsc0 parameter file (*45*−*47*). The models were solvated in a 10 Å box of TIP3P water using standard Amber 9.0 Leap rules to hydrate the systems. Potassium counterions were added for overall charge neutrality. The systems were heated slowly and equilibrated for 250 ps with gradual removal of positional restraints on the DNA following this protocol: (i) minimize water, (ii) 50 ps MD (T = 100 K) holding DNA fixed (100 kcal mol^{-1} Å), (iii) minimize water with DNA fixed (100 kcal mol^{-1} Å), (iv) minimize total system, (v) 50 ps MD (T = 100 K) holding DNA fixed (100 kcal mol^{-1} Å), (vi) 50 ps MD (T = 300 K) holding DNA fixed (100 kcal mol^{-1} Å), (vii) 50 ps MD (T = 300 K) holding DNA fixed (50 kcal mol^{-1} Å), (viii) 50 ps MD (T = 300 K) holding DNA fixed (10 kcal mol^{-1} Å), and (ix) 50 ps MD (T = 300 K) holding DNA fixed (1 kcal mol^{-1} Å). After the equilibration phase, an unconstrained production phase was then initiated and continued for 20 ns. Production runs of 20 ns after final equilibrium were used to obtain the average structures (200 snapshots in the last 2 ns), which were fully minimized. Simulations were performed in the isothermic isobaric ensemble (P = 1 atm, and T = 300 K). Periodic boundary conditions and the particle mesh Ewald algorithm were used. A 2.0 fs time step was used with bonds involving hydrogen atoms frozen using SHAKE. Molecular dynamics calculations were conducted with the AMBER

Table 1: Comparison of Na^+ and K^+ Concentrations for Half-Maximal Folding ($K_{0.5}$) and Hill Coefficients (n) Determined from Titrations of Cation-Induced Folding of Tel22 and 2-AP−Tel22 Oligodeoxynucleotides[a]

		A_{295} or CD_{295}[b]		F_{370}	
cation	oligonucleotide	$K_{0.5}$ (mM)	n	$K_{0.5}$ (mM)	n
Na^+	Tel22	3.09 ± 0.05	2.8 ± 0.1		
		2.93 ± 0.04[b]	2.8 ± 0.1	na[c]	
	AP1	5.9 ± 0.1	2.7 ± 0.1	8.3 ± 0.3	1.9 ± 0.1
	AP7	8.3 ± 0.08	2.3 ± 0.04	4.0 ± 0.1	3.1 ± 0.2
	AP13	4.2 ± 0.1	1.9 ± 0.1	3.7 ± 0.2	2.1 ± 0.2
	AP19	3.7 ± 0.1	1.3 ± 0.1	3.7 ± 0.2	2.8 ± 0.4
K^+	Tel22	0.253 ± 0.003	1.54 ± 0.03		
		0.256 ± 0.003[b]	1.54 ± 0.03	na[c]	
	AP1	0.50 ± 0.02	1.30 ± 0.05	0.50 ± 0.02	2.1 ± 0.2
	AP7	0.35 ± 0.004	1.73 ± 0.03	0.29 ± 0.03	1.5 ± 0.2
	AP13	0.167 ± 0.004	1.50 ± 0.05	0.20 ± 0.01	4.5 ± 1.3
	AP19	0.287 ± 0.005	1.74 ± 0.05	0.10 ± 0.006	8.9 ± 7.3

[a]Folding was assessed from changes in absorbance at 295 nm, fluorescence at 370 nm, and CD at 295 nm. The constants were derived by fitting the data in Figure 3 (fluorescence) or Figure 4 (CD and absorbance) to eq 4 using a nonlinear least-squares procedure. Errors are standard deviations of the fitted parameters. [b]Values estimated by measurement of CD at 295 nm. [c]Not applicable.

program sander. The trajectories were analyzed using the PTRAJ module in AMBER and visualized using Chimera (*48*). Solvent accessible surface areas (SASA) were computed from structural coordinates in PDB entry 143D for Tel22 in Na^+ (*14*) or the coordinates for the Tel22 hybrid-1 or hybrid-2 computational model using NACCESS version 2.1.1 (*49*).

RESULTS

Folding Monitored by UV Difference Spectroscopy. We initially compared folding isotherms for Na^+- and K^+-induced folding of the 2-AP-containing oligonucletotides with those for unmodified Tel22. Quadruplex formation results in extensive changes in DNA UV absorption with a characteristic increase in absorbance at ~295 nm. The results of these titrations are summarized in Table 1; the corresponding cation-dependent difference spectra and titration curves given as Supporting Information (Figure S1). As previously observed (*22*), the folding transitions for Tel22 were cooperative with Hill coefficients of ~1.5 in KCl and ~2.8 in NaCl and $K_{0.5}(Na^+) > K_{0.5}(K^+)$. Folding of 2-AP derivatives of Tel22 was also cooperative with respect to $[M^+]$, with $n(Na^+) > n(K^+)$ and $K_{0.5}(Na^+) > K_{0.5}(K^+)$. However, the values of the fitted parameters for some of the 2-AP derivatives were slightly different from the same parameters for folding unmodified Tel22. The most notable differences were a decrease in the n value of AP19 in NaCl, a nearly 2-fold increase in $K_{0.5}(Na^+)$ for AP7, and a 2-fold decrease in $K_{0.5}(K^+)$ for AP13 and AP19. These differences may reflect 2-AP-induced alterations in the ensemble of unfolded conformers, alterations in the conformation of the folded states, or a combination of the two (*50*). These differences in the binding parameters are not unexpected in view of the small differences in CD spectra of Tel22 and the four 2-AP derivatives in Na^+- and K^+-containing buffers along with minor differences in thermal stability of the folded structures that were previously described by Li et al. (Supporting Information in ref *27*). It should also be noted that these fitted constants are empirical descriptions of the coupling between cation binding and oligonucleotide folding rather than pure cation binding constants or folding equilibrium constants (*50*).

Fluorescence Emission Spectra of 2-AP Derivatives of Tel22. We next show cation-dependent changes in the 2-AP fluorescence emission spectra of the modified Tel22 oligonucleotides. Previous studies from our laboratory (*27*) showed that the fluorescence of 2-AP individually substituted for the four dA residues of Tel22 depends on the substitution site and the identity of the cation. These differences were attributed to differences in the positioning of the various loops connecting the G-quartets.

The emission spectra obtained in this study for the unfolded and folded structures are shown in Figure 2. All of the spectra exhibited maxima near 370 nm, irrespective of the folding state, cation, or sequential location of the fluorophore. This is expected on the basis of previous studies that show that the emission maximum of 2-AP is relatively insensitive to its local environment. However, the fluorescence quantum yield depended on the substitution position and on the cation and its concentration (Figure 2). This sensitivity of 2-AP quantum yield is expected on the basis of studies that show that stacking 2-AP with nearest-neighbor bases and solvent accessibility influence 2-AP emission intensity; in the study presented here, 2-AP at the 5′ end (e.g., AP1) has only a single neighboring nucleotide, whereas the other 2-AP residues positioned between T and G obviously have two neighbors and therefore exhibit greater quenching. It has also been shown that G is an especially effective quencher of 2-AP fluorescence in oligonucleotides by virtue of an electron transfer mechanism between G and 2-AP (*51*).

The relative effects of cation-induced folding on 2-AP emission intensities are summarized in Table 2. Na^+-induced folding of AP1 and AP13 exhibited quenching in the folded state, while folding of AP7 and AP19 resulted in enhanced fluorescence. In contrast, the fluorescence quantum yield of K^+-induced folding of the 2-AP−Tel22 derivatives was noticeably biphasic with respect to K^+ concentration. In 3 mM KCl, AP1, AP7, and AP19 exhibited increased emission relative to the unfolded state while AP13 fluorescence was quenched in 3 mM KCl (Table 2, column 3). In 100 mM KCl, the fluorescence of AP1 and AP13 was quenched but AP7 and AP19 exhibited increased fluorescence relative to the unfolded states (Table 2, column 4). The order of quenching in this study differs from that previously reported (*27*). In our previous study (in which the published spectra were determined at 5 °C), the order of emission intensity in Na^+ was as follows: AP7 > AP19 > AP1 > AP13. For K^+, the order was as follows: AP7 > AP1 ≈ AP19 > AP13. However, at 37 °C the order of intensities differed from that at 5 °C (J. Li and J. B. Chaires, unpublished data) and is the same as that observed in our experiments (conducted at 25 °C): AP7 > AP19 > AP1 > AP13 in Na^+ and AP7 > AP1 > AP19 > AP13 in K^+. These results suggest temperature-dependent conformational heterogeneity at positions 1 and 19 (loop 3).

To compare loop folding with G-quartet formation, we conducted cation titrations monitored by changes in UV absorption and 2-AP fluorescence. Titration curves of AP1, AP7, and AP13 in Na^+ monitored by fluorescence were approximately monophasic as shown in Figure 3A. The Na^+-induced fluorescence change of AP19 was slightly biphasic, with a relatively small degree of quenching (< 10%) apparent at up to ~1 mM NaCl, followed by a larger degree of fluorescence enhancement at higher NaCl concentrations. The n and $K_{0.5}$ values obtained by fitting the data to eq 4 are summarized in Table 1.

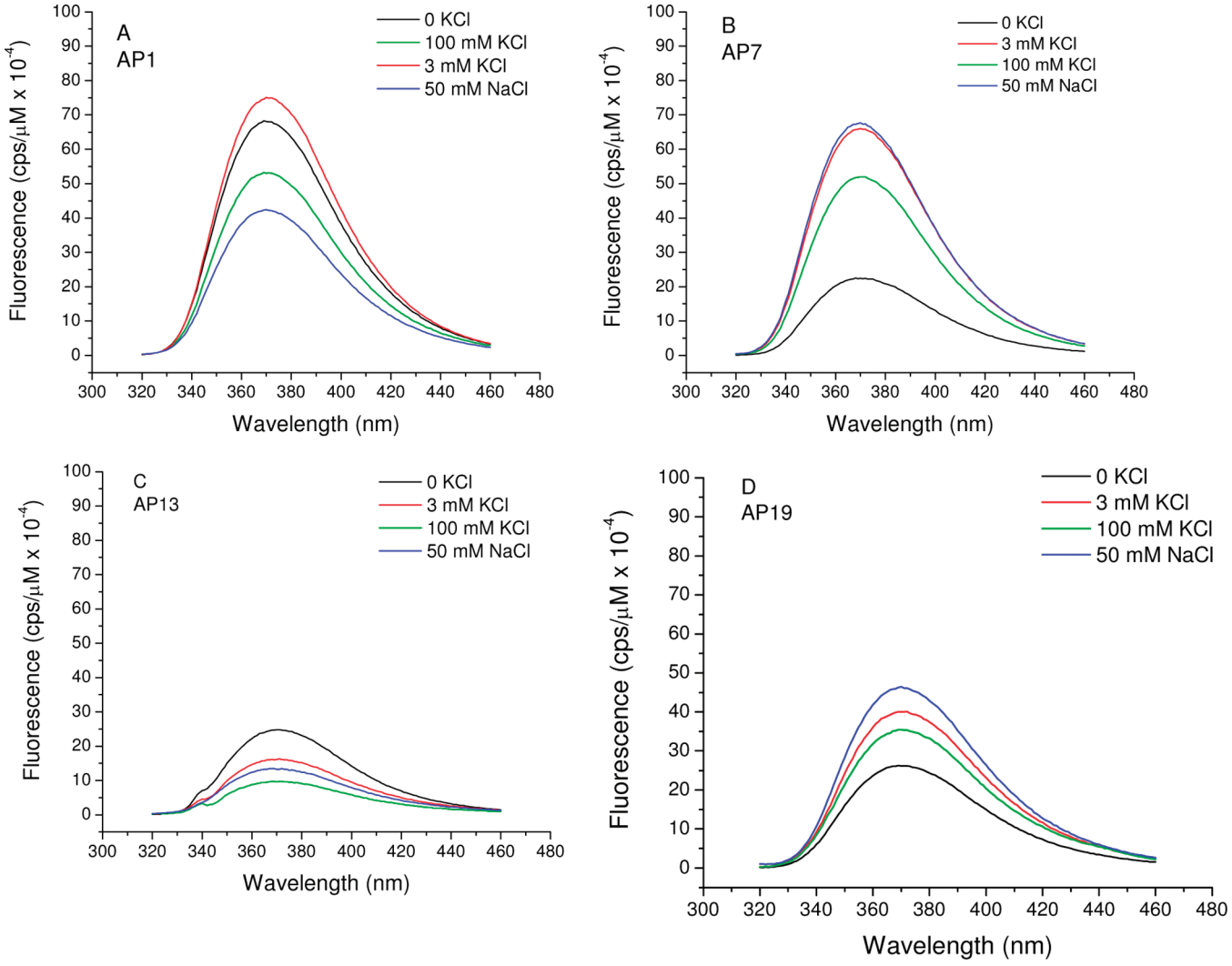

FIGURE 2: Na^+- and K^+-dependent fluorescence emission spectra of 2-AP derivatives of Tel22 as a function of cation concentration. Fluorescence intensities are normalized to 1 μM oligonucleotide and corrected for day-to-day variation in the fluorometer excitation lamp intensity by normalization to the intensity of the water Raman scatter peak at 340 nm. Conditions: 0.5−0.6 μM Tel22 in 10 mM Bu_4AmP and 1 mM EDTA (pH 7.0) at 25 °C. The excitation wavelength was 305 nm.

Table 2: Relative Changes in Fluorescence Emission at 370 nm Induced by Folding of 2-AP Derivatives of Tel22 in NaCl and KCl

	F/F_0[a]		
	50 mM NaCl	3 mM KCl	100 mM KCl
AP1	0.6	1.2	0.8
AP7	2.9	3	2.3
AP13	0.5	0.7	0.4
AP19	1.7	1.5	1.4

[a] F is the fluorescence intensity in the indicated salt, and F_0 is the fluorescence intensity in the absence of added salt. The values of F and F_0 were estimated from the emission spectra shown in Figure S1 of the Supporting Information.

The K^+ titration curves in Figure 3B reveal a clear biphasic dependence of emission intensity on K^+ concentration. AP1 and AP19 showed increases of ~50 and ~10% in fluorescence intensity up to ~1 mM KCl followed by quenching at higher KCl concentrations. K^+-induced folding of AP7 resulted in a 3.6-fold increase in fluorescence that was quenched at > 10 mM KCl. The AP13 fluorescence was quenched by ~20% at 1 mM KCl followed by nearly 100% near 100 mM KCl. Control experiments conducted with 2-AP showed that the fluorescence quantum yield of the free base is not affected by NaCl or KCl at concentrations up to at least 100 mM. Thus, we conclude from the biphasic titration curves that folding 2-AP−Tel22 derivatives in KCl generates at least two classes of K^+-binding sites. The high-affinity sites are undoubtedly located within the quadruplex channel. On the basis of molecular dynamics simulations presented below, the lower-affinity site involves residues dA1 and dT18.

Cation-Induced Changes in CD Spectra. In view of the biphasic fluorescence titration data in Figure 3B, we examined the dependence of CD changes of native Tel22 on M^+ concentration. Titrations with NaCl over the concentration range of 0−100 mM monitored by CD are consistent with a folding equilibrium consisting of two significant spectroscopic species as confirmed by analysis of the wavelength−Na^+ concentration data matrix by singular-value decomposition (SVD) analysis (Figure S2 of the Supporting Information). In contrast, CD titrations of K^+-induced folding showed distinct spectral heterogeneity as a function of KCl concentration as indicated by the lack of isodichroic points throughout the titration (Figure 4A). Figure 4B shows changes in ellipticity at 295 nm for Tel22 over the KCl concentration range of 0−100 mM. Fitting the titration

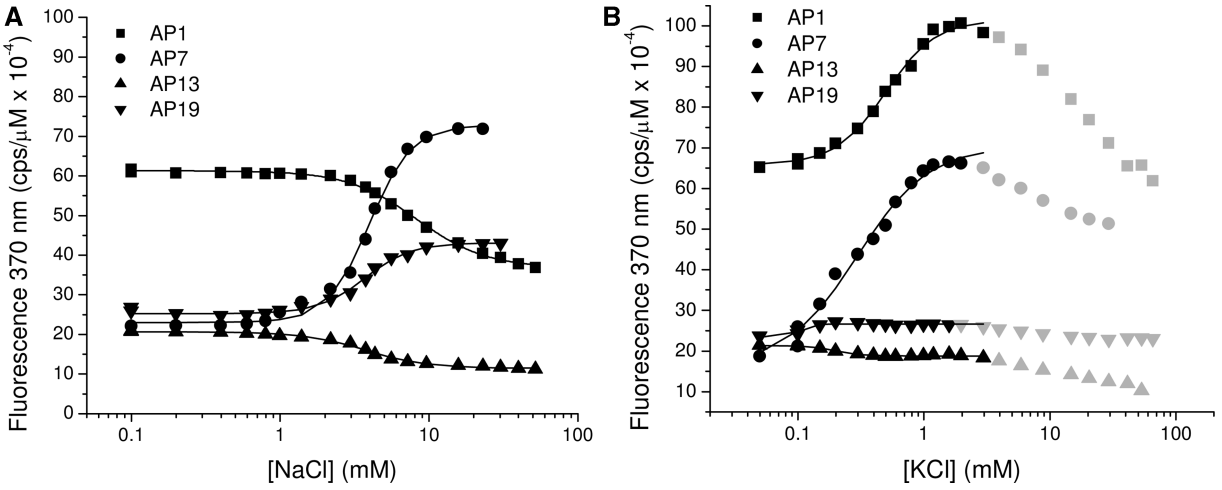

FIGURE 3: Titration curves for cation-induced folding of 2-AP derivatives of Tel22 assessed by changes in fluorescence emission at 370 nm. Panel A shows the dependence of the fluorescence intensity on NaCl concentration, and panel B shows the dependence of the fluorescence intensity on KCl concentration for the derivatives of Tel22 substituted with 2-AP at the indicated positions. The points represent the experimental fluorescence intensities (normalized to an oligonucleotide concentration of 1 μM), and the line shows the fit of the data points to eq 3 determined by nonlinear least-squares fitting as described in the text. The data points were corrected for day-to-day variations in excitation intensity. The data points colored gray in panel B were not included in the fitting. The optimized fitting parameters are given in Table 1. Conditions: 0.7−1.0 μM Tel22 in 10 mM Bu_4AmP and 1 mM EDTA (pH 7.0) at 25 °C. The excitation wavelength was 305 nm.

curve to eq 4 gave a Hill coefficient of 1.5 and a $K_{0.5}$ of 0.26 mM KCl. Analysis of the wavelength−concentration data matrix set by SVD showed clear evidence of three significant spectroscopic species throughout the titration (Figure 4A). Evolving factor analysis allowed calculation of theoretical CD spectra for the starting species, the low-K^+ species, and the high-K^+ species (Figure 4C) and their KCl-dependent concentration profiles (Figure 4D). The shape of the CD spectrum of the 1 mM KCl species resembles that of the final state formed at higher KCl concentrations, but the intensity is lower. Both shapes are characteristic of hybrid-type structures rather than basket-type structures. Details of the SVD analysis of Na^+ and K^+ titrations are given in Figures S3 and S4 of the Supporting Information.

KCl-Dependent ^{1}H NMR Spectra of Tel22. To confirm the presence of a K^+ concentration-dependent conformational switch suggested by the fluorescence and CD titrations in Figures 3B and 4C, we compared the one-dimensional (1D) ^{1}H NMR spectra of Tel22 at lower and higher K^+ concentrations. Figure 5 shows the imino proton region of the NMR spectra of Tel22 (179 μM) at 1.5 and 37 mM KCl at 10 and 25 °C. The spectrum at 37 mM K^+ represents the "end point" and comprises 20 different frequencies, and by intensities > 24 protons. This is roughly twice the number expected for a single three-stack G-quadruplex such as the hybrid-1 or hybrid-2 form (*21*). Indeed, the spectrum appears to be the superposition of two overlapping states in slow exchange. For example, the resonances near 10.8 ppm appear to represent species in a ratio of approximately 2:1 as assessed by the relative peak areas of the cluster. A similar spectrum was also recorded in the presence of 100 mM K^+. In the absence of K^+, only broad unresolved resonances were observed (data not shown). Sharpening of resonances from 10 to 25 °C implies that the GN1H resonances are not exchanging significantly under these conditions; i.e., the quartets are stable even at 25 °C and low salt.

Cation-Induced Folding Kinetics Monitored by UV Absorbance Changes. Kinetic experiments for cation-induced folding of the 2-AP−Tel22 derivatives determined by rapid scanning stopped-flow spectrophotometry gave kinetic constants similar to those previously published for native Tel22 (*22*). Briefly, folding of the 2-AP−Tel22 derivatives induced by 100 mM NaCl took place in three steps with relaxation times of 20−60 ms, ~0.5 s, and ~10 s (Figure S5 of the Supporting Information). The time constants for these steps are similar to those previously observed with Tel22. K^+-induced folding of the 2-AP derivatives assessed by UV absorbance occurred in a single-exponential process with relaxation times of ~40 ms in 50 mM KCl for all of the 2-AP derivatives (Figure S7 of the Supporting Information). The observation of a single relaxation is the same as previously observed with native Tel22. From these two sets of experiments, we conclude that folding of the 2-AP derivatives and native Tel22 as assessed by changes in UV absorbance occurs via the same kinetic mechanisms expressed in eqs 1 and 2.

The kinetics of both Na^+- and K^+-induced folding of the 2-AP−Tel22 derivatives determined by 2-AP fluorescence was multiphasic with the changes extending for milliseconds to minutes. To capture the complete range of folding times, we utilized both stopped-flow and manual mixing methods. These two procedures generated data sets for the folding kinetics of the four 2-AP derivatives in 100 mM NaCl, 3 mM KCl, and 50 mM KCl. Representative progress curves are reproduced in Figure 6 for folding of AP19 in 100 mM NaCl and in Figure 7 for folding of AP7 in 3 and 50 mM KCl. The corresponding progress curves for Na^+- and K^+-induced folding of the remaining 2-AP derivatives of Tel22 are given as Supporting Information (Figures S6 and S7). The relaxation times and signal amplitudes derived from these experiments are summarized in Table 3.

NaCl-Dependent Folding Monitored by 2-AP Fluorescence. Folding the 2-AP derivatives of Tel22 in 100 mM NaCl determined by stopped-flow fluorescence revealed that a significant fraction of the fluorescence change occurred during the ~0.1 s instrumental dead time for all of the 2-AP derivatives. For AP1 and AP13, the fluorescence initially decreased, while AP7 and AP19 exhibited an initial rapid increase in fluorescence. Independent experiments showed that changes in UV absorption at 295 nm were complete in < 2 s under these conditions for all of the 2-AP-containing oligonucleotides (Figure S5 of the Supporting Information). Thus, we conclude that the rapid initial "burst" fluorescence change results primarily from formation of the

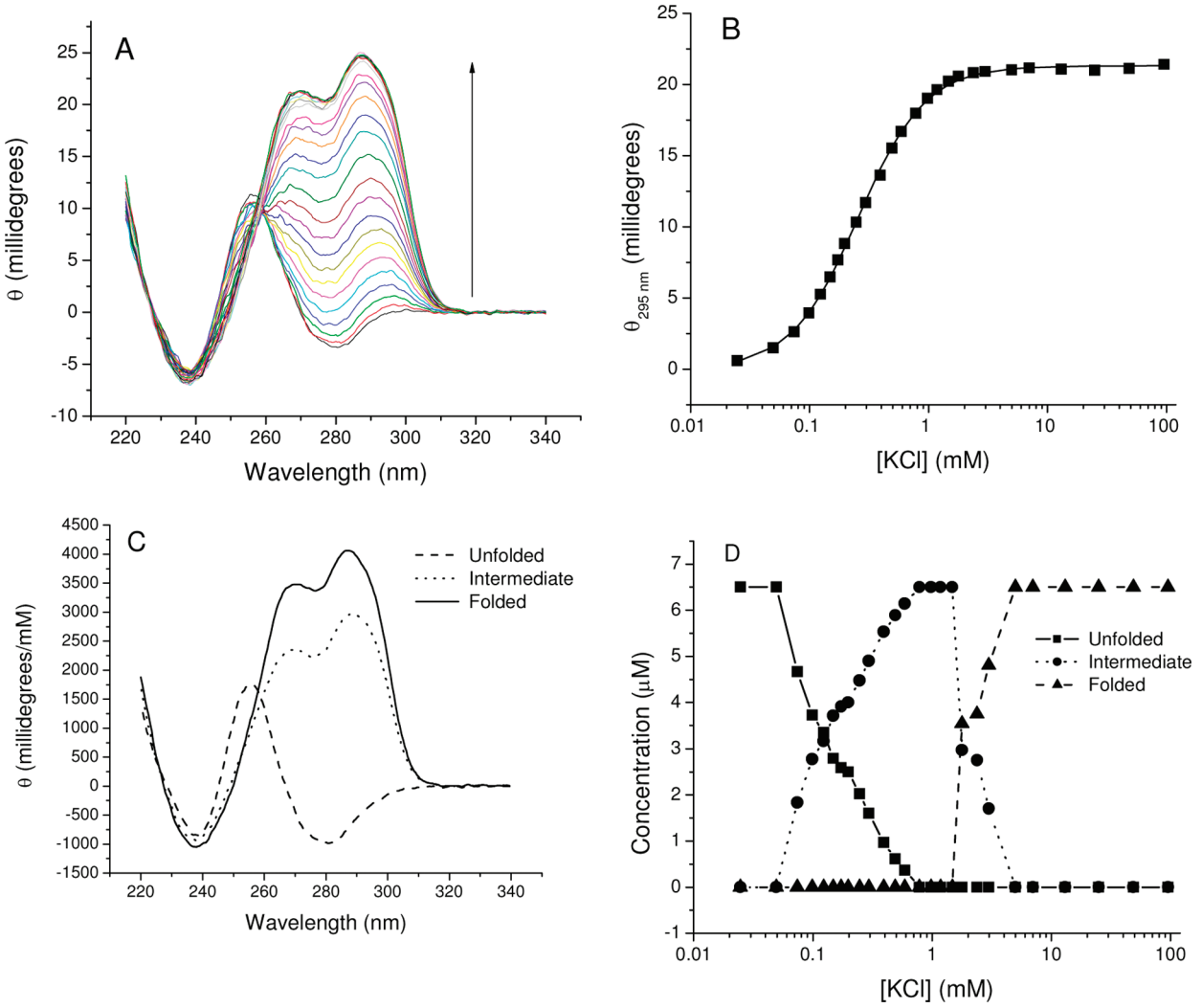

FIGURE 4: Titration of Tel22 with KCl determined by CD. Panel A shows the CD spectra for Tel22 at various KCl concentrations. The spectra were generated by titration with KCl between the concentrations of 0 and ~100 mM. The vertical arrows indicate the direction of the changes with an increase in K^+ concentration. The cation concentrations are summarized in Table S1 of the Supporting Information. Panel B shows the values of ellipticity at 295 nm as a function of salt concentration. The lines show the least-squares fit of the data points to eq 3. The optimized fitting parameters are given in Table 1 for these curves. Panel C shows the theoretical CD spectra of the unfolded, intermediate, and folded states calculated by the model-free evolving factor analytical procedure as described in the text. Panel D shows the concentration profiles of the three significant spectroscopic species. The detailed results of the SVD analysis are given in the Supporting Information. Conditions: 6.7 μM Tel22 in 10 mM Bu_4AmP and 1 mM EDTA (pH 7.0) at 25 °C.

quadruplex stack. The observation of position-specific increases or decreases in fluorescence quantum yield suggests that the 2-AP residues located within these different positions undergo either stacking (in the case of quenching) or unstacking (in the case of fluorescence enhancement) relative to the unfolded state upon formation of the initial folding intermediate (I or I1 in eq 1 or eq 2) (*26*).

In addition to these fast changes in fluorescence, we also observed relatively slow, position-specific changes in emission that occurred over time periods of up to several minutes. The progress curves for AP1, AP7, and AP13 are shown in Figure S6 of the Supporting Information, and the kinetic constants derived from these progress curves are listed in Table 3. In summary, AP1, AP7, and AP13 exhibited slow, biphasic changes in emission with relaxation times ranging from 1.5 to 14 s (determined from the stopped-flow experiments) and slower changes with τ values of 30−56 s determined by manual mixing. Depending on the loop position, both positive (fluorescence enhancement) and negative (fluorescence quenching) amplitudes were observed. Folding of AP19 (loop 3) was more complex as it occurred with three slow relaxations with τ values of ~4, 10, and 45 s and signal amplitude changes of negative to positive to negative (Figure 6). The significantly different kinetic constants and directions of the fluorescence changes for the individual 2-AP derivatives suggest that the initial, rapidly formed ensemble of intermediates in NaCl slowly adjust loop conformation to form the stable basket topology.

The relaxation times described above for Na^+-induced changes in fluorescence can be compared with those determined by changes in UV absorption for folding of the 2-AP-containing oligonucleotides induced by this cation. As with native Tel22, UV spectroscopic assessment of folding of the 2-AP derivatives in 100 mM NaCl revealed a rapid step (τ values of 12−43 ms, depending on the site of substitution) and two slow steps with τ values of 0.4−1 and 5−10 s (Figure S5 of the Supporting Information). Comparison of these time constants with those listed in Table 3 for folding assessed by fluorescence changes reveals that the folding rates assessed by the two different spectroscopic probes do not correlate exactly, suggesting that changes UV absorption and fluorescence intensity monitor different microscopic details

of the structural changes. For example, it seems likely that the relatively minor, slow UV absorption changes in the 295 nm spectral region predominantly reflect subtle differences in G-quartet geometry, while the changes in 2-AP fluorescence emission may also be sensitive to local changes involving the conformation of the 2-AP residue itself. It is likely that the rate and magnitude of these changes will be different for different loops. This supposition is supported by the K^+-induced folding experiments that consisted of a single major kinetic process as detected by UV spectroscopy between 275 and 320 nm but clearly exhibited a series of relatively slow changes in fluorescence emission intensity (discussed below).

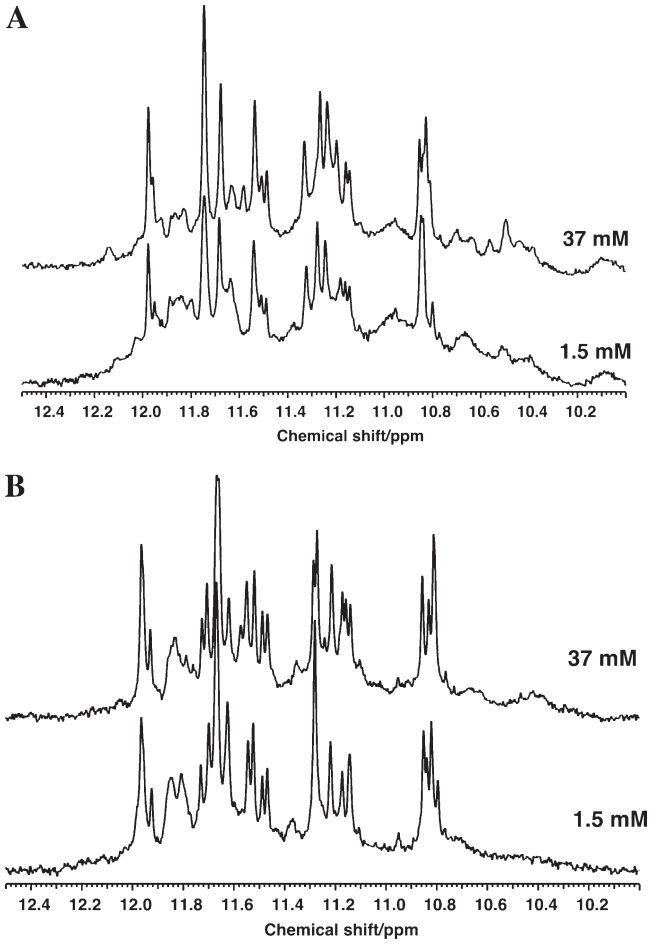

FIGURE 5: ^{1}H NMR spectra of Tel22 as a function of KCl concentration showing the imino proton region of the NMR spectra of Tel22 (178 μM) at 1.5 and 37 mM KCl at 10 (A) and 25 °C (B).

The relatively slow adjustments in tertiary structure may be interpreted to indicate a "rugged folding landscape" for quadruplex formation in which a number of kinetically accessible structures are sampled prior to slow relaxation to a thermodynamically stable structure or mixture of structures. Along this line, it is noteworthy that the triphasic adjustment of the conformation of AP19 in NaCl indicates that this loop 3 residue undergoes a more complex series of conformational rearrangements than the 2-AP residues in loops 1 and 2. This could indicate that loop 3 undergoes a substantial change in topology as suggested by our proposed folding mechanism in which the basket conformation is formed from a hypothetical chair-type intermediate (*22*).

KCl-Dependent Folding Monitored by 2-AP Fluorescence. In view of the heterogeneity of the folding equilibria observed in equilibrium titrations, we determined progress curves for folding of 2-AP−Tel22 intermediates at low (3 mM) and higher (50 mM) KCl concentrations. Surprisingly, in view of the single kinetic process observed for K^+-dependent folding of Tel22 monitored by UV absorbance changes, the kinetics of fluorescence changes in KCl was heterogeneous, displaying relaxations over a period of milliseconds to minutes at all substitution positions. Representative progress curves for these fluorescence changes for AP7 are shown in Figure 7. In manual mixing experiments in 3 mM KCl, all of the 2-AP derivatives exhibited relatively rapid initial changes in fluorescence during the ~5 s dead time. Comparison of the progress curves with parallel stopped-flow UV experiments (shown in Figure S7 of the Supporting Information) conducted under similar conditions suggests that these rapid fluorescence changes are associated with G-quartet formation and stacking. In addition, AP1, AP13, and AP7 exhibited relatively slow single-exponential fluorescence quenching with τ values of ~500−900 s, reflecting site-specific adjustment of the loop conformation (Table 3 and Figure S8 of the Supporting Information). In contrast, AP7 exhibited a

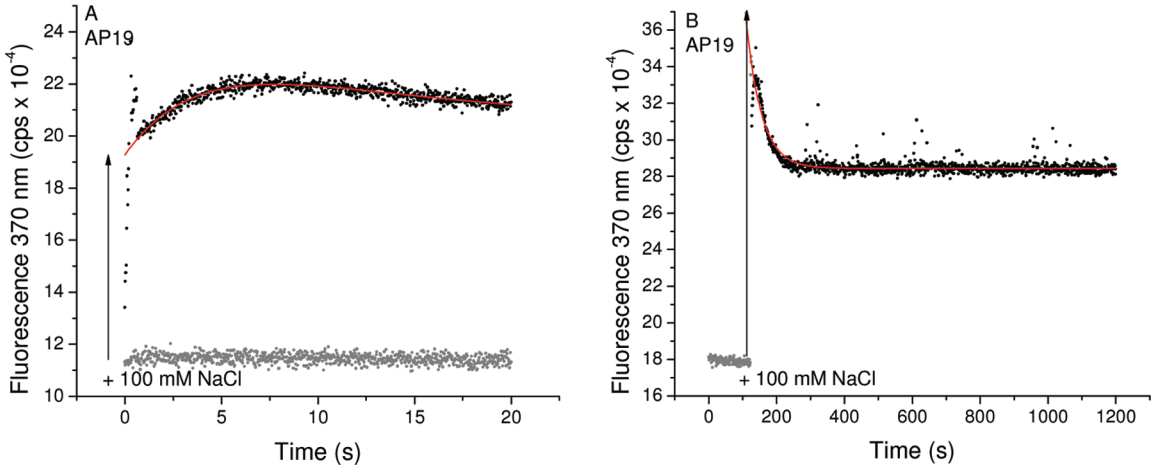

FIGURE 6: Kinetics of changes in 2-AP fluorescence accompanying Na^+-induced folding of the AP19 derivative of Tel22. The data in panel A were obtained by stopped-flow mixing, and the data in panel B were obtained by a manual mixing procedure. The data points colored gray show the fluorescence intensity at 370 nm immediately prior to addition of NaCl (100 mM after mixing) to initiate folding, and the points colored black show the fluorescence intensity after mixing with NaCl. Note the rapid change in emission that occurred during the mixing period (vertical arrow). The red line shows the best fit of the data points to a sum of two exponentials using the optimized parameters listed in Table 3.

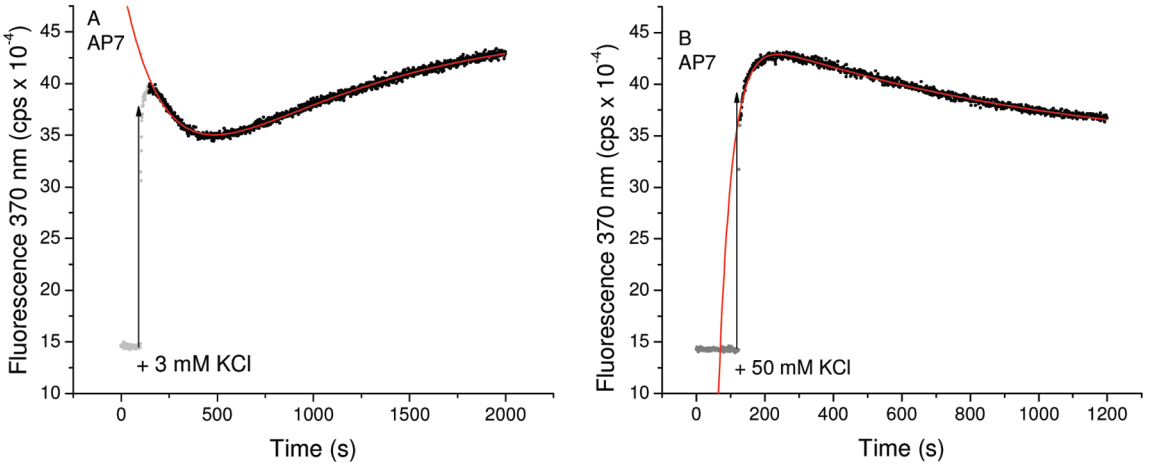

FIGURE 7: Kinetics of changes in 2-AP fluorescence accompanying K^+-induced folding of the AP7 (loop 1) Tel22 oligonucleotide. Panel A shows the folding progress curve in 3 mM KCl, and panel B shows a progress curve for folding in 50 mM KCl. In both panels, the data points colored gray show the fluorescence intensity at 370 nm immediately prior to addition of KCl to initiate the folding process (vertical arrow). The points colored black show progress curves after addition of KCl, and the red line shows the fit to the data points by a nonlinear least-squares method using the optimized parameters listed in Table 3.

Table 3: Fitted Kinetic Parameters for NaCl- and KCl-Induced Folding of 2-AP Derivatives of Tel22 Determined by Fluorescence[a]

position	y_0	A_1	τ_1 (s)	A_2	τ_2 (s)
Stopped-Flow Mixing with 100 mM NaCl					
AP1	28.84 ± 0.02	7.42 ± 0.06	4.04 ± 0.06	0	
AP7	28.06 ± 0.24	−5.2 ± 0.2	13 ± 1	0	
AP13	6.87 ± 0.01	1.89 ± 0.05	1.47 ± 0.06	0	
AP19	20.57 ± 0.41	−7.2 ± 6.7	4.3 ± 1.4	5.9 ± 6.4	9.4 ± 6.2
Manual Mixing with 100 mM NaCl					
AP1	28.54 ± 0.01	23.9 ± 1.1	56 ± 1	0	
AP7	35.07 ± 0.01	−400 ± 50	30.3 ± 0.8	0	
AP13	8.32 ± 0.00	1050.00 ± 1010.00	35 ± 4	0	
AP19	28.43 ± 0.01	92 ± 9	45 ± 1	0	
Manual Mixing with 3 mM KCl					
AP1	71.73 ± 0.05	−31.94 ± 0.04	975 ± 4	0	
AP7	45.6 ± 0.2	−24.1 ± 0.6	913 ± 33	28.9 ± 0.6	234 ± 6
AP13	11.23 ± 0.01	−2.65 ± 0.03	557 ± 11	0	
AP19	29.36 ± 0.03	−6.69 ± 0.03	788 ± 13	0	
Stopped-Flow Mixing with 50 mM KCl					
AP1	31.5 ± 0.9	3.7 ± 0.1	1.08 ± 0.07	5.4 ± 0.8	25 ± 6
AP7	26.55 ± 0.04	−4.12 ± 0.06	5.3 ± 0.2	0	
AP13	6.94 ± 0.05	2.18 ± 0.04	10.8 ± 0.5	0	
AP19	13 ± 12	1.2 ± 0.1	1.8 ± 0.3	6 ± 11	92 ± 215
Manual Mixing with 50 mM KCl					
AP1	38.22 ± 0.01	−8.7 ± 0.1	173 ± 2	0	
AP7	32.87 ± 0.22	−182 ± 14	37 ± 1	13.5 ± 0.1	923 ± 32
AP13	6.15 ± 0.00	20 ± 1.5	41 ± 1	27.7 ± 0.4	97 ± 3
AP19	29.79 ± 0.08	−7.1 ± 0.3	480 ± 30	0	

[a]The optimized kinetic constants associated with the progress curves in Figures 6, 7, S6, and S7 were determined by fitting the progress curves to a sum of one or two exponentials by nonlinear least-squares analysis as described in the text. A_2 values of zero indicate that the data set was adequately fit by one exponential. Positive values of the pre-exponential factor A indicate enhanced fluorescence, and negative values indicate fluorescence quenching. Errors are standard deviations of the fitted parameters.

triphasic response: an initial rapid, relatively large enhancement of fluorescence followed by a decrease in fluorescence which was then followed by a fluorescence increase; these slower changes were characterized by τ values of ~200 and ~900 s, respectively (Figure 7C).

Multistep kinetic changes in fluorescence were also noted when the 2-AP derivatives were folded in 50 mM KCl. Stopped-flow mixing experiments covering a 20 s time period revealed an initial rapid fluorescence enhancement for AP7 and AP19 and a small degree of quenching for AP1 and AP13. These rapid changes were followed by relatively slow fluorescence enhancement for AP7 and slow quenching for AP13 and AP19. There was little initial fluorescence change for AP1 on folding in 50 mM KCl, suggesting that initial formation of G-quartets in this case does not result in a significant change in the AP1 environment relative to the unfolded state. The observed slow biphasic increase−decrease sequence of changes in fluorescence signal suggests a complex repositioning of AP1 after quartet stacking. The time constants associated with these intermediate steps were 1−10 and 25−90 s. Manual mixing experiments with 50 mM KCl revealed further slow adjustments in fluorescence occurring with τ values of ~40 to ~900 s. These results suggest that the initial, rapidly formed ensemble of conformers slowly rearranges by adjusting loop folding to give a stable mixture of conformers. A major conclusion from the fluorescence studies of K^+-driven folding of 2-AP−Tel22 derivatives is that monitoring the folding reaction by site-specific fluorescence changes reveals intermediate steps in folding that did not give appreciable changes in UV absorbance in the 270−320 nm wavelength range.

Fluorescence Depolarization. Assessment of the depolarization of fluorescence when a fluorophore is excited with polarized light can reveal the rotational mobility of the fluorophore provided that the lifetime of the excited state is comparable to the rotational relaxation time of the fluorophore. P, the steady-state degree of emission polarization, is defined as $(I_{\parallel} - I_{\perp})/(I_{\parallel} + I_{\perp})$, where $I_{\parallel}$ and $I_{\perp}$ represent the intensities of the emitted light in directions parallel and perpendicular to the direction of polarization of the exciting radiation, respectively. P consists of two components: (a) an intrinsic polarization (P_0) that depends on the geometric relationship between the excitation and emission dipoles and (b) a component that depends on the rotational motion of the fluorophore. For macromolecules, a change in P may result from a change in the local mobility of the fluorophore and/or a change in rotational diffusion resulting

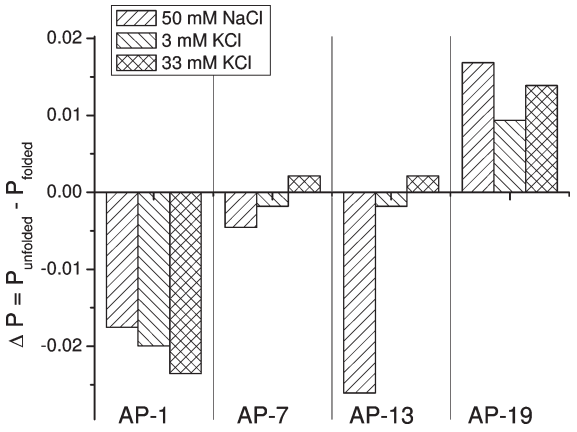

FIGURE 8: Changes in fluorescence polarization measured at 370 nm induced by cation-induced folding of 2-AP derivatives of Tel22. Folding was initiated via rapid addition of a small volume of a 3 M salt solution to a rapidly stirring solution of oligonucleotide to give the final salt concentrations indicated in each panel.

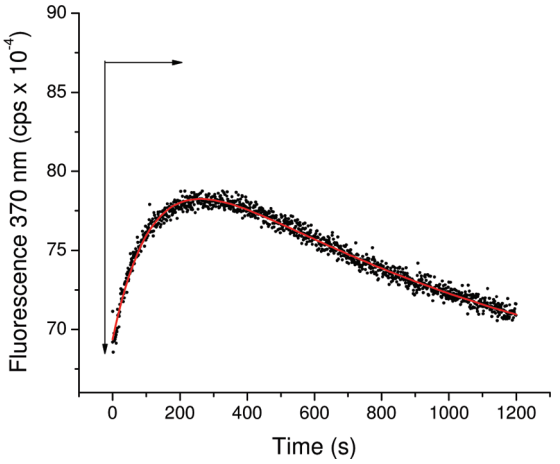

FIGURE 9: Na^+-K^+ exchange kinetics for the AP7 derivative of Tel22. The exchange reaction was initiated via addition of KCl from a 3 M stock solution to a rapidly stirred solution of the oligonucleotide pre-equilibrated with 75 mM NaCl. The data points show the change in fluorescence upon addition of 150 mM KCl. The horizontal arrow indicates the starting value of the fluorescence in NaCl immediately prior to the addition of KCl. The vertical arrows indicate the rapid fluorescence change that occurred during the ~5 s mixing time. The red line shows the fit of the experimental data to a double-exponential relaxation using the optimized parameters listed in Table 4.

from a change in hydrodynamic volume, e.g., one accompanying a transition from a random coil to a compact, folded structure.

The average steady-state values of P were within the range of 0.07−0.14 depending on the 2-AP derivative and the nature of the cation. These relatively small P values are expected given the short lifetime of the 2-AP excited states in quadruplexes [~0.5 ns (*52*)] and the rotational relaxation time of the folded quadruplex [calculated to be 4 ns at 25 °C using Hydropro (*53*)]. Except for AP7 in NaCl and KCl and AP-13 in KCl, significant changes in P were induced by folding for each oligonucleotide (summarized in Figure 8). Folding of AP1 in NaCl and KCl and folding of AP13 in NaCl were characterized by an increase in P, while folding of AP19 was accompanied by a decrease in P. Thus, motion of AP1 and AP13 in NaCl appeared to be more restricted in the folded ensemble than in the unfolded ensemble, while AP19 gained mobility in the folding transition.

Na^+-K^+ Exchange Kinetics. We expected that a comparison of fluorescence changes accompanying the $Na^+ \rightarrow K^+$ cation exchange reaction for the four 2-AP−Tel22 derivatives might indicate which loops undergo a change in orientation in the transition from the Na^+-antiparallel basket structure to the K^+-dependent mixture of topologies. A representative progress curve for cation exchange in AP7 is shown in Figure 9, and the fitted time constants associated with the exchange of Na^+ for K^+ for each of the four 2-AP derivatives of Tel22 are listed in Table 4. The progress curves for cation exchange with AP1, AP13, and AP19 are reproduced in Figure S9 of the Supporting Information. For all of the 2-AP−Tel22 derivatives, there was an initial rapid fluorescence change that occurred during the ~5 s mixing time when KCl was rapidly added to the NaCl-folded structures. For AP1, the fluorescence intensity rapidly increased followed by a slower decrease that fit first-order kinetics. For AP7, AP13, and AP19, an initial rapid quenching in fluorescence was observed. For AP13, the rapid step was followed by slow quenching, while for AP19, the rapid quenching step was followed by slow fluorescence enhancement. AP7 uniquely exhibited biphasic slow fluorescence changes in which enhanced fluorescence was followed by quenching (Figure 9). This complex series of fluorescence changes for AP7 suggests that when switching from the Na^+-bound basket conformation to the K^+-bound conformations, loop 1 undergoes an additional isomerization that does not occur with loops 2 and 3. We speculate that this additional step may result from a switch in loop 1 in the Na^+ basket from an antiparallel topology to the parallel arrangement characteristic of the hybrid-1 structure. As shown below, our molecular dynamics simulation suggests a mechanism of stabilization of the hybrid-1 structure by specific binding of an additional potassium cation.

Table 4: Fitted Kinetic Constants for Na^+-K^+ Exchange for 2-AP−Tel22 Derivatives[a]

	y_0	A_1	τ_1 (s)	A_2	τ_2 (s)
AP1	27.74 ± 0.03	7.63 ± 0.04	364 ± 5	0	
AP7	64.3 ± 0.7	−14.60 ± 0.03	122 ± 3	19.9 ± 0.4	1086 ± 86
AP13	8.47 ± 0.03	1.92 ± 0.04	189 ± 10	0	
AP19	33.88 ± 0.03	−9.74 ± 0.04	296 ± 3	0	

[a]The optimal kinetic constants describing the progress curves in Figures 9 and S8 were determined by fitting the data sets to a sum of one or two exponentials by nonlinear least-squares analysis as described in the text. A_2 values of zero indicate that the data set was adequately described by a single exponential. Positive values of A indicate enhanced fluorescence, and negative values indicate fluorescence quenching. Errors are standard deviations of the fitted parameters.

Comparing the data obtained in monitoring fluorescence changes within loop 1 with the results of our study in which CD was used to monitor the Na−K exchange reaction for native Tel22 (*24*) is worthwhile. The CD change induced by switching cations occurs in at least three steps: an initial rapid step within the 5 s mixing time followed by slower steps with τ values of ~50 and ~800 s. The rapid CD change was interpreted to reflect an exchange of K^+ for Na^+ within the central channel of the quadruplex, a process known to take place on a microsecond time scale (*54*, *55*). The intermediates associated with the two slower steps were suggested to consist of transiently formed triplex structures.

Molecular Modeling. Numerous studies (reviewed in ref *54*) have shown that K^+ ions are bound within the quadruplex central channel by coordination to the O6 atoms of the G

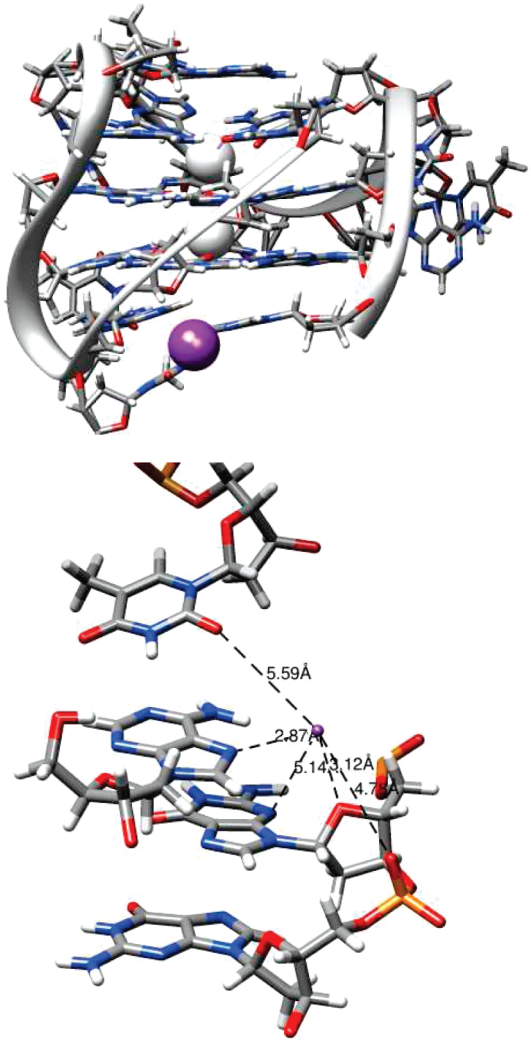

FIGURE 10: Hypothetical external K^+-binding site in Tel22 hybrid-1 topology. The figure was generated from a snapshot taken at the conclusion of the molecular dynamics simulation of the hybrid-1 form of Tel22 described in the text. The gray spheres represent the channel-bound K^+ atoms, and the purple sphere shows the position of the externally bound K^+. The bottom panel shows a detailed representation of the K^+-binding site with potential coordinating groups (and their distances from K^+): dT18−O2 (5.59 Å), dA1−N7 (2.87 Å), dG20−O4′ (3.12 Å), dG20−N3 (5.14 Å), and dG21−O1P (4.78 Å). The figures were constructed using Chimera (*41*).

residues; because of their larger size, these K^+ atoms are located between the individual tetrads rather than within the tetrad plane as suggested for Na^+. A number of studies also show that in certain quadruplex structures, cations are bound within the connecting loops. As described in more detail in Discussion, these coordination sites often involve thymine O2 atoms. The biphasic changes in loop fluorescence observed in our K^+ titrations (Figures 2 and 3) imply the existence of K^+ coordination sites in addition to the channel sites. To further investigate this possibility, we examined the K^+ distribution in unrestrained molecular dynamics trajectories calculated for models with various Tel22 topologies. In addition to the expected K^+-binding sites in the quadruplex core, we noted an increase in K^+ ion density exclusively within a region of the hybrid-1 model adjacent to A1. This region was manifested by extended K^+ residence times of up to approximately 2.5 ns compared to other sites; a similar increase in K^+ density was not found in the hybrid-2 structure. These results suggest the existence of an "external" K^+-binding site specific for the hybrid-1 structure. Figure 10 shows characteristics of this site.

DISCUSSION

This study compares the kinetics of quadruplex folding previously deduced from UV-dependent stopped-flow studies with the folding kinetics monitored by loop-specific changes in 2-AP fluorescence. We expected that these folding-induced fluorescence changes would report the dynamics of formation of stable loops and might reflect changes in strand topology. The telomeric model oligodeoxynucleotide chosen for the study, Tel22, has a well-defined solution structure in Na^+ that consists of an antiparallel basket with two lateral loops and one diagonal loop (Figure 1A). In contrast, in solution in the presence of the physiologically interesting cation K^+, Tel22 consists of a mixture of unknown topologies with different loop arrangements and strand orientations (*17*, *19*, *21*, *56*, *57*).

Our experimental strategy involved comparing the folding equilibria and kinetics of derivatives of Tel22 in NaCl and KCl in which the 5′ dA residue and the three loop dA residues were serially replaced with the fluorescent adenine analogue, 2-aminopurine. Factors that influence 2-AP fluorescence quantum yield have been extensively studied. Among the most important of these factors is base stacking which quenches 2-AP fluorescence; it has also been reported that the 2-AP quantum yield is sensitive to the presence of nearby cations (*28*). Previous studies from our laboratory (*27*) showed that the fluorescence of 2-AP−Tel22 derivatives is sensitive to differences in quadruplex folding topology induced by different cations, and moreover, the studies provide a rational approach to distinguishing among various quadruplex folding topologies in solution.

Loop Dynamics. Our earlier work on the cation-induced folding of Tel22 as assessed by changes in UV absorption indicated a multistep folding mechanism (*22*). In both Na^+ and K^+, a folding intermediate, possibly hairpin structure(s), was formed in a relatively fast step that became rate-limiting at high cation concentrations. In K^+, there were no significant changes in UV absorption in the 275−320 nm range subsequent to this rapid step. In Na^+, however, two slower UV relaxations indicated the presence of additional kinetic intermediates on the pathway to formation of the basket topology prevalent with this cation. A similar mechanism was apparent for folding TT-Tel22-A in Na^+, a sequence known to form the hybrid-1 structure in a K^+ solution (*20*). These results show that the folding mechanism determined by monitoring changes in UV absorption depends on the cation and is independent of the flanking sequences for Tel22 and these 5′ and 3′ variants. Furthermore, since TT-Tel22-A forms the hybrid-1 topology in K^+ whereas Tel22 in K^+ forms a mixture of structures, the folding mechanism determined by changes in UV absorption in the 275−320 nm range is apparently independent of the nature of the final equilibrium ensemble of folded structures.

The 2-AP fluorescence changes observed here support a multistep mechanism for Tel22 folding induced by both Na^+ and K^+, and the fluorescence data indicate that the slower steps involve loop rearrangements. K^+-driven folding exhibits a series of slow steps that were not evident in the UV kinetic studies but were obvious from fluorescence changes in the loops. In addition, the observation of sequential positive and negative changes in fluorescence emission intensity induced in KCl-dependent folding for AP19 (Figure 5) and for folding of AP1, AP7, and AP19 in NaCl (Figure 6) supports a sequential folding pathway (eq 2) as

opposed to a branched pathway (eq 6):

$$\begin{array}{c} U \leftrightarrow I \rightarrow F1 \\ \downarrow \\ F2 \end{array} \quad (6)$$

This conclusion is illustrated by a simulation of the reaction sequences given in eqs 2 and 5 with the assumption that each species is characterized by a different fluorescence quantum yield which shows that only eq 2 gives a reaction profile characterized by increasing and decreasing exponentials (Figure S10 of the Supporting Information).

Folding Equilibria. Our previous equilibrium titrations monitored by cation-induced changes in UV absorption suggested the presence of small amounts of intermediate species, possibly partially folded structures and/or structures containing an incomplete complement of bound cations. In this study, the fluorescence experiments conducted in KCl with the 2-AP−Tel22 derivatives and the CD studies conducted with Tel22 reveal the presence of species with different fluorescence and CD properties as a function of K^+ concentration. It is likely that these species are fully folded, stable quadruplexes with differing topographies rather than partially folded intermediates. It is clear from the fluorescence KCl titration curves in Figure 3B taken in conjunction with the KCl-dependent NMR spectra in Figure 5 that a different structural ensemble is present in ~1 mM K^+ compared to that at >10 mM K^+ for a period of several hours after the cation solution is mixed with the unfolded oligonucleotide at 25 °C. The solution structures of these conformers and their relative concentrations are unknown, but a possible interpretation is that the predominant conformers are the hybrid-1 and hybrid-2 structures. On the basis of the presence of an additional K^+-binding site unique to the hybrid-1 structure suggested by our molecular dynamics simulations, the prevailing conformer at low K^+ concentrations may be the hybrid-2 structure (which lacks this site).

External Potassium-Binding Sites in Quadruplexes. Several studies have been published that provide precedent for the existence of cation-binding sites within the loops of G-quadruplex structures (see ref *54* for a comprehensive review). For example, Jing et al. (*58*, *59*) reported that K^+-induced formation of a unimolecular quadruplex by the anti-HIV oligonucleotide d[GTGGT(GGGT)$_3$] is a two-step process in which one K^+ is incorporated into the two-stack quadruplex core to form a high-affinity complex while two K^+ ions bind in a slower reaction to loop sites with lower affinity. These investigators observed biphasic folding isotherms in CD and UV titrations of K^+ similar to those presented here (Figures 2 and 3). For titrations of Na^+-induced folding, the isotherms were monophasic, suggesting that Na^+ binds only within the quadruplex channel but not to loop sites for the anti-HIV quadruplex. In another example of cation binding within a loop, Marathias and Bolton (*60*) characterized K^+-induced folding of the thrombin-binding aptamer d(GGTTGGTGTGGTTGG). These authors reported two K^+-binding sites: one within the quadruplex channel and one in a loop region involving the thymine O2 atoms and the O6 atoms of one of the G-quartets. More recently, Phan et al. (*21*) determined the solution structure of the two human telomeric sequences, d[TAGGG(TTAGGG)$_3$] and d[TAGGG(TTAGGG)$_3$TT], by NMR. In a K^+ solution, the former consisted of 70% hybrid-1 and the latter consisted of 70% hybrid-2. K^+-induced changes in NOEs for the longer sequence were explained by coordination of K^+ (but not Na^+) within the T12-T13-A14 loop. A molecular dynamics simulation indicated that the T1, T12, and A14 residues and the O6 atom of the adjacent quartet chelate one K^+ ion.

Cation-binding sites located within quadruplex loops have also been demonstrated in bimolecular and tetramolecular quadruplexes. Bouaziz et al. (*61*) determined the solution structure of the bimolecular quadruplex formed by d[$G_3CT_4G_3C$] in Na^+ and K^+. The two different cations stabilize structures with different loop configurations. Modeling identified potential cation-binding sites specific for K^+ involving the O2 atoms of T6 and T8, the sugar ring O atom of T7, T8, and G9, and the backbone O atoms of the T7-T8 and G8-G9 pairs located within the two T_4 loops. In pointing out the potential functional significance of loop cation binding, the authors suggested that these K^+ atoms binding to these sites resulted in "a defined loop architecture whose outwardly pointing groups provide a unique folded topology that can target potential receptor sites" (*61*).

The crystal structure of d($G_4T_4G_4$), which forms a bimolecular structure consisting of four G-stacks, reveals three K^+ atoms coordinated between quartets and two K^+ atoms bound within the T-loops (*62*). Recently, Ida and Wu (*55*) provided NMR evidence of Na^+ binding within the T4 loops of d($G_4T_4G_4$). The coordination site was proposed to involve the four O6 atoms of guanine residues of the last quartet, the O2 atom of a loop thymine, and a water molecule.

In an example of K^+-dependent conformational heterogeneity in monomeric G-quadruplexes, Lee et al. (*63*) analyzed the distribution of conformational states in a solid-state, single-molecule FRET system. They presented evidence for three interconvertible states: an unfolded conformation and two folded conformations, each characterized by a different FRET efficiency. The proportion of each conformation depended on K^+ concentration and temperature. One folded state was favored at low K^+ concentrations (0.1−2 mM), and a different one was favored at 100 mM KCl. The folding kinetics observed when 2 mM KCl was added to a bulk solution of the unfolded structure was biphasic with τ values of 8.8 and 253 s, relaxation times which are similar to the relaxation times for the K^+-dependent loop conformational changes noted in our study. It was suggested that the slow step involved a change in strand topology. The two studies are therefore complementary in that both independently point to a K^+-dependent conformational isomerization of quadruplex structures.

Loop Structures. We next turn to a structural rationalization for the changes in the fluorescence properties of 2-AP induced by folding in NaCl, 3 mM KCl, and 30 mM KCl. For reference, Table 5 provides a qualitative summary of the changes in the fluorescence properties associated with each substitution position. It is important to note at the outset that signals such as fluorescence are measured with respect to the unfolded oligonucleotide, which probably consists under our starting conditions of an ensemble of partially collapsed states with varying degrees of interaction between adjacent bases rather than an extended structure dictated by the electrostatic repulsion between phosphate groups. An additional complicating factor is the known heterogeneity of the folded state of Tel22 in KCl. The spectroscopic signals observed for the starting and final states will represent an average of the signals for each conformer weighted according to its relative concentration. This structural heterogeneity almost certainly falls into two categories: microheterogeneity at the site of the 2-AP residue and topological heterogeneity due to different folded structures in the presence of K^+. The observed changes in the fluorescence properties of a

Table 5: Summary of the Direction of Fluorescence Changes for Cation-Induced Folding of Tel22

oligo-nucleotide	location	stacked[a]	mobility	change[b] in fluorescence intensity (U → F)	change[b] in polarization (U → F)	change[b] in fluorescence intensity for kinetic steps
				Na^+ (50 mM)		
AP1	core	yes	fixed	↓	↑	↓↓↑[c]
AP7	loop 1	no	mobile	↑	↑	↑↑
AP13	loop 2	yes	fixed	↓	↑	↓↓
AP19	loop 3	yes	mobile	↑	↓	↓↑
				K^+ (3 mM)		
AP1	core			↓	↑	↑↓→
AP7	loop 1			↑	→	↑↓↓
AP13	loop 2			↓	→	↑↓↓
AP19	loop 3			↑	↓	↑↓↑
				K^+ (33 mM)		
AP1	core			→	↑	↑↓
AP7	loop 1			↑	→	↑↓
AP13	loop 2			↓	→	↓
AP19	loop 3			↑	↓	↑↓

[a]Determined from the NMR structure of Tel22 (*14*). [b]Key: ↑, increase; ↓, decrease; →, no significant change. [c]In order of steps 1, 2, and 3.

fluorophore in solution will thus be an average weighted in proportion to the conformers present in the starting and final states and the extent of the change associated with each conformational change. Since the mechanisms driving quenching and changes in polarization are different, there may not always be a direct correlation between the two parameters. The net change in either fluorescence quantum yield or polarization is therefore not predictable without prior knowledge of the degree of change for a given conformer and its concentration within the sample. With these caveats, we next discuss the relationship between the folded structures and the fluorescence quantum yield and polarization at each position in the basket, hybrid-1, and hybrid-2 topologies.

5′ Cap (*A1*). In the basket conformation, the topology in Na^+ solution, A1 stacks over G2 (*14*). It is the least solvent-exposed of the four dA residues (SASA = 104 Å^2). The NMR-derived structures in PDB entry 143D (*14*) suggest that A1 is relatively fixed with respect to the molecular framework. In the titrations with Na^+, the AP1 fluorescence was quenched, which is consistent with an increase in the extent of base stacking interactions relative to the unfolded state. The level of fluorescence polarization increased on folding, indicating that AP1 becomes less mobile on folding which is consistent with the restricted movement suggested by the ensemble of NMR structures. The triphasic folding transition assessed by fluorescence is similar that observed previously by UV absorption, suggesting that the changes in fluorescence reflect changes in the local environment at the 5′ position resulting from relatively slow optimization of the tertiary structure in the vicinity of the first G-quartet. In addition, these changes were reported by the (rather small) changes in UV absorption (*22*).

The interpretation of the fluorescence changes in KCl is not straightforward because, as noted, Tel22 in K^+ exists as a mixture of unknown topologies in unknown proportions. However, it is of interest to compare the hybrid-1 and hybrid-2 computational models of Tel22. In the hybrid-2 model, A1 is sandwiched between T12 and G10. It is the least exposed of all dA residues (SASA = 85 Å^2). Experimentally, we found an increase in AP1 fluorescence on folding up to ~3 mM KCl, and an increase in the level of steady-state polarization. The increase in the level of polarization is consistent with sequestration of AP1 relative to the unfolded state, but the observed increase in quantum yield is at odds with an increase in the extent of stacking. An increase in the level of polarization and a corresponding increase in quantum yield may seem inconsistent; however, we suggest that folding could lead to a decrease in rotational motion of AP1 due to its sequestration while simultaneously providing less stacking interactions in the folded state. This suggests the hybrid-2 model does not account for the behavior of AP1 at low KCl concentrations. The folding kinetics in 3 mM KCl was biphasic, exhibiting a small decrease followed by a large increase in fluorescence. The absence of a large rapid change in emission (probably associated with quartet formation) suggests that the environment of AP1 in the initially formed structure is not much different than in the unfolded ensemble; consequently, most of the fluorescence change takes place during the final positioning of AP1.

A1 also forms a 5′ cap in the hybrid-1 model. It is stacked with G20 and has intermediate solvent accessibility (SASA = 183 Å^2). At high K^+ concentrations, there was net quenching fluorescence. Polarization increased, suggesting that 2-AP1 experiences a net decrease in flexibility on folding to its equilibrium conformational ensemble at high K^+ concentrations. Thus, the fluorescence data are consistent with the predictions suggested by biasing the conformational equilibrium toward the hybrid-1 state.

Loop 1 (*T5-T6-A7*). In the Na^+ basket form, A7 is located in a lateral loop and is not stacked with other bases. A7 is the most exposed to solvent (250 Å^2) of the four dA residues. The NMR-derived structures in PDB entry 143D (*14*) indicate that a variety of positions is consistent with the data, suggesting flexibility at this position. Indeed, the fluorescence changes on folding are consistent with higher flexibility within loop 1 since folding was accompanied by an increase in quantum yield and little or no change in polarization relative to the unfolded state. These results

are consistent with weakensed stacking interactions. Loop formation was biphasic, with both steps resulting in increased fluorescence, suggesting formation of folding intermediates with a decreased level of base stacking.

In the hybrid-2 model, A7 is located in a lateral loop where it is imperfectly stacked on the G4-G8-G16-G22 quartet. It has a relatively high exposure (SASA = 215 Å^2). In 3 mM K^+, folding was characterized by an increase in quantum yield and no net change in polarization. The kinetics of the changes in emission was triphasic, suggesting successive intermediates characterized by decreases in fluorescence with the final equilibrium ensemble showing an increase in fluorescence.

In the hybrid-1 model, AP7 stacks on top of the G4-G10-G14-G20 quartet. Its SASA is 236 Å^2. In 30 mM K^+, AP7 exhibited an identical set of changes as in 3 mM KCl except that the rapid phase in fluorescence emission, corresponding to quartet formation, was not apparent, probably having occurred during the dead time of the instrument.

Loop 2 (*T11-T12-A13*). In Na^+, loop 2 is in a diagonal arrangement with A13 stacked over G22. A13 is relatively exposed (SASA = 170 Å^2). The ensemble of NMR structures indicates that this residue has restricted mobility. The Na^+-induced changes in AP13 emission are consistent with this picture. There was a net decrease in quantum yield on folding and an increase in the level of polarization. The kinetics of the change in emission was biphasic, with two intermediates of lower fluorescence. This is consistent with formation of the diagonal loop occurring in a stepwise fashion with two kinetic intermediates.

In hybrid-2, A13 in loop 2 stacks on top of the G2-G10-G14-G20 tetrad. It has intermediate exposure to solvent (SASA = 139 Å^2). Experimentally, in 3 mM K^+, loop 2 was formed with a net decrease in fluorescence and a negligible change in polarization. The kinetics of the fluorescence change was triphasic with the intermediates showing successively decreased, decreased, and increased fluorescence.

A13 in the hybrid-1 structure is stacked over G22. The accessible surface area is ~223 Å^2. In 30 mM K^+, formation of loop 2 occurred with a net decrease in fluorescence, suggesting an increased level of stacking with respect to the unfolded state, little or no change in polarization, and a single-step decrease in fluorescence.

Loop 3 (*T17-T18-A19*). In the basket structure, A19 is stacked over G16 and exhibits flexibility as suggested by the variety of orientations evident in the NMR-generated conformational ensemble. SASA is 140 Å^2. The folding-induced increase in fluorescence and the decrease in the level of polarization are consistent with this structure. As with loops 1 and 2, the kinetics of formation of lateral loop 3 was biphasic, showing an increase followed by a decrease in fluorescence.

In hybrid-2, A19 packs into a groove. It is relatively more exposed to solvent (SASA = 217 Å^2) and is not stacked with other bases. In 3 mM K^+, formation of loop 3 was accompanied by an increase in fluorescence and a decrease in the level of polarization, consistent with unstacking and an increase in rotational mobility. The kinetics of the fluorescence emission change was triphasic, suggesting changes in loop conformation that are associated with variations in base stacking.

In hybrid-1, A19 lies under the G2-G8-G16-G20 tetrad and over T18. It is relatively inaccessible to solvent (SASA = 135 Å^2). Folding in 100 mM KCl occurred with an increase in fluorescence and a decrease in the level of polarization relative to those of the unfolded ensemble. These observations are consistent with an unstacking of A19 relative to the unfolded state.

In conclusion, the observed position-specific changes in 2-AP fluorescence correlate well with those expected from the antiparallel basket structure formed in Na^+. Detailed correlation of the changes in fluorescence with specific structures in KCl is not possible due to the topological heterogeneity of the folded state. Nevertheless, it is clear from the differential effects of KCl concentration that changes in the concentration of this cation lead to different populations of conformers. Similarly, the $K^+ \rightarrow Na^+$ conformational switch occurs on a slow time scale, suggesting that both reactions require adjustment of strand topologies.

Cation-Driven Allosterism in Quadruplex DNA. The studies reported here show that changes in cation identity and concentration induce changes in quadruplex tertiary structure. These observations suggest the possibility of K^+-driven allosteric control mechanisms. Our studies define the energetics and kinetics of these conformational switches as driven by either a change in cation from Na^+ to K^+ or a change in K^+ concentration.

The ability of biological macromolecules to undergo conformational changes in response to ligand binding is fundamental to the theory of allosteric regulation. The original allosteric theory of Monod, Wyman, and Changeaux (*64*) postulated that regulatory proteins exist in equilibrium between two conformations with different intrinsic activities and different affinities for regulatory molecules. According to thermodynamic linkage theory, binding a molecule to a site specific for one conformation will bias the population of conformers toward a state with a characteristic activity profile. Recently, the mechanism of allostery has been reformulated to take into account current theories of protein structure (*65*, *66*) which postulate that proteins exist as an ensemble of conformational states in which relatively high-energy states may be transiently visited due to thermal motion. An allosteric regulatory molecule may bind to one of these rare states, thereby lowering its free energy and thus increasing its representation in the population. In this model, understanding the molecular basis of allosteric regulation requires knowledge of the relative populations of individual states and their rates of interconversion.

It is less widely appreciated, but nonetheless equally important, to recognize that polynucleotides may also utilize allosteric mechanisms for functional regulation (*67*, *68*). As with proteins, ligand binding to a particular DNA conformation may drive structural changes that may result in changes in the affinity of the DNA sequence for effector molecules such as small ligands, polymerases, transcription factors, etc. Several examples of nucleic acid allosterism have recently been summarized (*68*). Among the nonclassical structural motifs amenable to study of allosterically mediated DNA regulatory mechanisms are conformational transitions in G-quadruplex structures. These structures display a high degree of conformational heterogeneity in which the individual topographies are separated by relatively low energy barriers. These features make G-quadruplex structures attractive candidates for the evolution of sensitive and facile regulatory mechanisms.

CONCLUSIONS

We demonstrated that 2-AP fluorescence is a sensitive monitor of the equilibria and kinetics of changes in the conformation of specific loop regions in model oligonucleotides that mimic the human telomeric sequence. Changes in 2-AP fluorescence

resulting from K^+ binding clearly indicate the presence of high-affinity binding sites within the quadruplex channel and low-affinity binding sites specific for K^+. Molecular dynamics simulations revealed a cation-binding site specific for the hybrid-1 form of the human telomeric sequence that involves the A1 residue. This model suggests that elevated K^+ concentrations will increase loop rigidity and stabilize a particular topography. We propose that this low-affinity site falls within the classical definition of an allosteric site. Thus, a K^+-dependent switching mechanism could be utilized to control quadruplex tertiary structure, thereby favoring the binding of conformation-specific effector molecules.

ACKNOWLEDGMENT

We thank Prof. A. N. Lane for assistance with NMR experiments and the reviewers for thoughtful comments and suggestions.

SUPPORTING INFORMATION AVAILABLE

Figures S1−S10 and Table S1 illustrating spectrophotometric titrations, kinetic data, SVD analyses, and simulated fluorescence progress curves. This material is available free of charge via the Internet at http://pubs.acs.org.

REFERENCES

1. Huppert, J. L. (2008) Hunting G-quadruplexes. *Biochimie 90*, 1140–1148.
2. Huppert, J. L. (2008) Four-stranded nucleic acids: Structure, function and targeting of G-quadruplexes. *Chem. Soc. Rev. 37*, 1375–1384.
3. McEachern, M. J., Krauskopf, A., and Blackburn, E. H. (2000) Telomeres and their control. *Annu. Rev. Genet. 34*, 331–358.
4. Wright, W. E., Tesmer, V. M., Huffman, K. E., Levene, S. D., and Shay, J. W. (1997) Normal human chromosomes have long G-rich telomeric overhangs at one end. *Genes Dev. 11*, 2801–2809.
5. Verdun, R. E., and Karlseder, J. (2007) Replication and protection of telomeres. *Nature 447*, 924–931.
6. Palm, W., and de Lange, T. (2008) How shelterin protects mammalian telomeres. *Annu. Rev. Genet. 42*, 301–334.
7. Collado, M., Blasco, M. A., and Serrano, M. (2007) Cellular senescence in cancer and aging. *Cell 130*, 223–233.
8. Deng, Y., Chan, S. S., and Chang, S. (2008) Telomere dysfunction and tumour suppression: The senescence connection. *Nat. Rev. Cancer 8*, 450–458.
9. Schaffitzel, C., Berger, I., Postberg, J., Hanes, J., Lipps, H. J., and Pluckthun, A. (2001) In vitro generated antibodies specific for telomeric guanine-quadruplex DNA react with *Stylonychia lemnae* macronuclei. *Proc. Natl. Acad. Sci. U.S.A. 98*, 8572–8577.
10. Burge, S., Parkinson, G. N., Hazel, P., Todd, A. K., and Neidle, S. (2006) Quadruplex DNA: Sequence, topology and structure. *Nucleic Acids Res. 34*, 5402–5415.
11. Patel, D. J., Phan, A. T., and Kuryavyi, V. (2007) Human telomere, oncogenic promoter and 5′-UTR G-quadruplexes: Diverse higher order DNA and RNA targets for cancer therapeutics. *Nucleic Acids Res. 35*, 7429–7455.
12. Dai, J., Carver, M., and Yang, D. (2008) Polymorphism of human telomeric quadruplex structures. *Biochimie 8*, 1172–1183.
13. Lane, A. N., Chaires, J. B., Gray, R. D., and Trent, J. O. (2008) Stability and kinetics of G-quadruplex structures. *Nucleic Acids Res. 36*, 5482–5515.
14. Wang, Y., and Patel, D. J. (1993) Solution structure of the human telomeric repeat $d[AG_3(T_2AG_3)_3]$ G-tetraplex. *Structure 1*, 263–282.
15. Parkinson, G. N., Lee, M. P., and Neidle, S. (2002) Crystal structure of parallel quadruplexes from human telomeric DNA. *Nature 417*, 876–880.
16. Phan, A. T., and Patel, D. J. (2003) Two-repeat human telomeric d(TAGGGTTAGGGT) sequence forms interconverting parallel and antiparallel G-quadruplexes in solution: Distinct topologies, thermodynamic properties, and folding/unfolding kinetics. *J. Am. Chem. Soc. 125*, 15021–15027.
17. Ambrus, A., Chen, D., Dai, J., Bialis, T., Jones, R. A., and Yang, D. (2006) Human telomeric sequence forms a hybrid-type intramolecular G-quadruplex structure with mixed parallel/antiparallel strands in potassium solution. *Nucleic Acids Res. 34*, 2723–2735.
18. He, Y., Neumann, R. D., and Panyutin, I. G. (2004) Intramolecular quadruplex conformation of human telomeric DNA assessed with ^{125}I-radioprobing. *Nucleic Acids Res. 32*, 5359–5367.
19. Xu, Y., Noguchi, Y., and Sugiyama, H. (2006) The new models of the human telomere $d[AGGG(TTAGGG)_3]$ in K^+ solution. *Bioorg. Med. Chem. 14*, 5584–5591.
20. Luu, K. N., Phan, A. T., Kuryavyi, V., Lacroix, L., and Patel, D. J. (2006) Structure of the human telomere in K^+ solution: An intramolecular (3 + 1) G-quadruplex scaffold. *J. Am. Chem. Soc. 128*, 9963–9970.
21. Phan, A. T., Kuryavyi, V., Luu, K. N., and Patel, D. J. (2007) Structure of two intramolecular G-quadruplexes formed by natural human telomere sequences in K^+ solution. *Nucleic Acids Res. 35*, 6517–6525.
22. Gray, R. D., and Chaires, J. B. (2008) Kinetics and mechanism of K^+- and Na^+-induced folding of models of human telomeric DNA into G-quadruplex structures. *Nucleic Acids Res. 36*, 4191–4203.
23. Hud, N. V., Smith, F. W., Anet, F. A. L., and Feigon, J. (1996) The selectivity for K^+ versus Na^+ in DNA quadruplexes is dominated by relative free energies of hydration: A thermodynamic analysis by ^{1}H NMR. *Biochemistry 35*, 15383–15390.
24. Gray, R. D., Li, J., and Chaires, J. B. (2009) Energetics and kinetics of a conformational switch in G-quadruplex DNA. *J. Phys. Chem. B 113*, 2676–2683.
25. Hall, K. B., and Williams, D. J. (2004) Dynamics of the IRE RNA hairpin loop probed by 2-aminopurine fluorescence and stochastic dynamics simulations. *RNA 10*, 34–47.
26. Jean, J. M., and Hall, K. B. (2004) Stacking-unstacking dynamics of oligodeoxynucleotide trimers. *Biochemistry 43*, 10277–10284.
27. Li, J., Correia, J. J., Wang, L., Trent, J. O., and Chaires, J. B. (2005) Not so crystal clear: The structure of the human telomere G-quadruplex in solution differs from that present in a crystal. *Nucleic Acids Res. 33*, 4649–4659.
28. Ballin, J. D., Bharill, S., Fialcowitz-White, E. J., Gryczynski, I., Gryczynski, Z., and Wilson, G. M. (2007) Site-specific variations in RNA folding thermodynamics visualized by 2-aminopurine fluorescence. *Biochemistry 46*, 13948–13960.
29. Ballin, J. D., Prevas, J. P., Bharill, S., Gryczynski, I., Gryczynski, Z., and Wilson, G. M. (2008) Local RNA conformational dynamics revealed by 2-aminopurine solvent accessibility. *Biochemistry 47*, 7043–7052.
30. Stivers, J. T. (1998) 2-Aminopurine fluorescence studies of base stacking interactions at abasic sites in DNA: Metal-ion and base sequence effects. *Nucleic Acids Res. 26*, 3837–3844.
31. Menger, M., Eckstein, F., and Porschke, D. (2000) Multiple conformational states of the hammerhead ribozyme, broad time range of relaxation and topology of dynamics. *Nucleic Acids Res. 28*, 4428–4434.
32. Jean, J. M., and Hall, K. B. (2001) 2-Aminopurine fluorescence quenching and lifetimes: Role of base stacking. *Proc. Natl. Acad. Sci. U.S.A. 98*, 37–41.
33. O'Neill, M. A., and Barton, J. K. (2002) 2-Aminopurine: A probe of structural dynamics and charge transfer in DNA and DNA:RNA hybrids. *J. Am. Chem. Soc. 124*, 13053–13066.
34. Jean, J. M., and Hall, K. B. (2002) 2-Aminopurine electronic structure and fluorescence properties in DNA. *Biochemistry 41*, 13152–13161.
35. Jean, J. M., and Krueger, B. P. (2006) Structural fluctuations and excitation transfer between adenine and 2-aminopurine in single-stranded deoxytrinucleotides. *J. Phys. Chem. B 110*, 2899–2909.
36. Wilson, J. N., Cho, Y., Tan, S., Cuppoletti, A., and Kool, E. T. (2008) Quenching of fluorescent nucleobases by neighboring DNA: The "insulator" concept. *ChemBioChem 9*, 279–285.
37. Hendler, R. W., and Shrager, R. I. (1994) Deconvolutions based on singular value decomposition and the pseudoinverse: A guide for beginners. *J. Biochem. Biophys. Methods 28*, 1–33.
38. DeSa, R. J., and Matheson, I. B. (2004) A practical approach to interpretation of singular value decomposition results. *Methods Enzymol. 384*, 1–8.
39. Sheardy, R. D., Suh, D., Kurzinsky, R., Doktycz, M. J., Benight, A. S., and Chaires, J. B. (1993) Sequence dependence of the free energy of B-Z junction formation in deoxyoligonucleotides. *J. Mol. Biol. 231*, 475–488.
40. Antonacci, C., Chaires, J. B., and Sheardy, R. D. (2007) Biophysical characterization of the human telomeric $(TTAGGG)_4$ repeat in a potassium solution. *Biochemistry 46*, 4654–4660.
41. Gampp, H., Maeder, M., Meyer, C. J., and Zuberbuhler, A. D. (1986) Calculation of equilibrium constants from multiwavelength spectroscopic data. IV. Model-free least-squares refinement by use of evolving factor analysis. *Talanta 33*, 943–951.

42. Piotto, M., Saudek, V., and Sklenar, V. (1992) Gradient-tailored excitation for single-quantum NMR spectroscopy of aqueous solutions. *J. Biomol. NMR 2*, 661–665.
43. Dai, J., Punchihewa, C., Ambrus, A., Chen, D., Jones, R. A., and Yang, D. (2007) Structure of the intramolecular human telomeric G-quadruplex in potassium solution: A novel adenine triple formation. *Nucleic Acids Res. 35*, 2440–2450.
44. Dai, J., Carver, M., Punchihewa, C., Jones, R. A., and Yang, D. (2007) Structure of the hybrid-2 type intramolecular human telomeric G-quadruplex in K^+ solution: Insights into structure polymorphism of the human telomeric sequence. *Nucleic Acids Res. 35*, 4927–4940.
45. Cornell, W. D., Cieplak, P., Bayly, C. I., Gould, I. R., Merz, K. M., Ferguson, D. M., Spellmeyer, D. C., Fox, T., Caldwell, J. W., and Kollman, P. A. (1995) A second generation force field for the simulation of proteins, nucleic acids, and organic molecules. *J. Am. Chem. Soc. 117*, 5179–5197.
46. Kollman, P. A., et al. (2006) AMBER 9 , University of California, San Francisco.
47. Perez, A., Marchan, I., Svozil, D., Sponer, J., Cheatham, T. E., III, Laughton, C. A., and Orozco, M. (2007) Refinement of the AMBER force field for nucleic acids: Improving the description of α/γ conformers. *Biophys. J. 92*, 3817–3829.
48. Pettersen, E. F., Goddard, T. D., Huang, C. C., Couch, G. S., Greenblatt, D. M., Meng, E. C., and Ferrin, T. E. (2004) UCSF Chimera: A visualization system for exploratory research and analysis. *J. Comput. Chem. 25*, 1605–1612.
49. Hubbard, S. J., and Thornton, J. M. (1993) NACCESS , University College, London.
50. Misra, V. K., and Draper, D. E. (2002) The linkage between magnesium binding and RNA folding. *J. Mol. Biol. 317*, 507–521.
51. Kelley, S. O., and Barton, J. K. (1999) Electron transfer between bases in double helical DNA. *Science* 375–381.
52. Kimura, T., Kawai, K., Fujitsuka, M., and Majima, T. (2007) Monitoring G-quadruplex structures and G-quadruplex-ligand complex using 2-aminopurine modified oligonucleotides. *Tetrahedron 63*, 3585–3590.
53. Garcia De La Torre, J., Huertas, M. L., and Carrasco, B. (2000) Calculation of hydrodynamic properties of globular proteins from their atomic-level structure. *Biophys. J. 78*, 719–730.
54. Hud, N. V., and Plavec, J. (2006) The role of cations in determining quadruplex structure and stability. In Quadruplex Nucleic Acids (Neidle, S., and Balasubramanian, S., Eds.) pp 100−130, Royal Society of Chemistry, Cambridge, U.K.
55. Ida, R., and Wu, G. (2008) Direct NMR detection of alkali metal ions bound to G-quadruplex DNA. *J. Am. Chem. Soc. 130*, 3590–3602.
56. Gaynutdinov, T. I., Neumann, R. D., and Panyutin, I. G. (2008) Iodine-125 radioprobing of intramolecular quadruplex conformation of human telomeric DNA in the presence of cationic porphyrin TMPyP4. *Int. J. Radiat. Biol. 84*, 984–990.
57. Gaynutdinov, T. I., Neumann, R. D., and Panyutin, I. G. (2008) Structural polymorphism of intramolecular quadruplex of human telomeric DNA: Effect of cations, quadruplex-binding drugs and flanking sequences. *Nucleic Acids Res. 36*, 4079–4087.
58. Jing, N., Gao, X., Rando, R. F., and Hogan, M. E. (1997) Potassium-induced loop conformational transition of a potent anti-HIV oligonucleotide. *J. Biomol. Struct. Dyn. 15*, 573–585.
59. Jing, N., Rando, R. F., Pommier, Y., and Hogan, M. E. (1997) Ion selective folding of loop domains in a potent anti-HIV oligonucleotide. *Biochemistry 36*, 12498–12505.
60. Marathias, V. M., and Bolton, P. H. (2000) Structures of the potassium-saturated, 2:1, and intermediate, 1:1, forms of a quadruplex DNA. *Nucleic Acids Res. 28*, 1969–1977.
61. Bouaziz, S., Kettani, A., and Patel, D. J. (1998) A K cation-induced conformational switch within a loop spanning segment of a DNA quadruplex containing G-G-G-C repeats. *J. Mol. Biol. 282*, 637–652.
62. Haider, S., Parkinson, G. N., and Neidle, S. (2002) Crystal structure of the potassium form of an *Oxytricha nova* G-quadruplex. *J. Mol. Biol. 320*, 189–200.
63. Lee, J. Y., Okumus, B., Kim, D. S., and Ha, T. (2005) Extreme conformational diversity in human telomeric DNA. *Proc. Natl. Acad. Sci. U.S.A. 102*, 18938–18943.
64. Monod, J., Wyman, J., and Changeux, J. P. (1965) On the nature of allosteric transitions: A plausible model. *J. Mol. Biol. 12*, 88–118.
65. Swain, J. F., and Gierasch, L. M. (2006) The changing landscape of protein allostery. *Curr. Opin. Struct. Biol. 16*, 102–108.
66. Tsai, C. J., Del Sol, A., and Nussinov, R. (2009) Protein allostery, signal transmission and dynamics: A classification scheme of allosteric mechanisms. *Mol. Biosyst. 5*, 207–216.
67. Chaires, J. B. (1985) Long-range allosteric effects on the B to Z equilibrium by daunomycin. *Biochemistry 24*, 7479–7486.
68. Chaires, J. B. (2008) Allostery: DNA does it, too. *ACS Chem. Biol. 3*, 207–209.